

THERMOELECTRIC MATERIAL PROPERTY MEASUREMENT  
FOR FLEXIBLE FILMS

by  
Courtney Hollar

A thesis  
submitted in partial fulfillment  
of the requirements for the degree of  
Master of Science in Mechanical Engineering  
Boise State University

August 2016

© 2016

Courtney Hollar

ALL RIGHTS RESERVED

BOISE STATE UNIVERSITY GRADUATE COLLEGE

**DEFENSE COMMITTEE AND FINAL READING APPROVALS**

of the thesis submitted by

Courtney Hollar

Thesis Title: Thermoelectric Material Property Measurement for Flexible Films

Date of Final Oral Examination: 14 June 2016

The following individuals read and discussed the thesis submitted by student Courtney Hollar, and they evaluated her presentation and response to questions during the final oral examination. They found that the student passed the final oral examination.

Yanliang Zhang, Ph.D. Chair, Supervisory Committee

Donald Plumlee, Ph.D. Member, Supervisory Committee

David Estrada, Ph.D. Member, Supervisory Committee

The final reading approval of the thesis was granted by Yanliang Zhang, Ph.D., Chair of the Supervisory Committee. The thesis was approved for the Graduate College by Jodi Chilson, M.F.A., Coordinator of Theses and Dissertations.

## ACKNOWLEDGEMENTS

Thank you to Dr. Zhang and my colleagues in the Advanced Energy Lab for helping me throughout this study by collaborating and providing me with new perspectives. In particular, I would like to thank Tony Varghese for his help and support throughout this thesis. I would also like to thank my thesis committee members, Dr. Plumlee and Dr. Estrada, for their mentorship.

I am appreciative of my family and Scooter as they continue to provide love and guidance throughout my life. I am very grateful to have the love and support of Khris and Lucy, who continue to encourage me throughout this chapter of my life. In addition, I am thankful of the support from both the Kohlmeier family and my friends.

## ABSTRACT

The market for wearable electronics and implantable medical devices continues to grow. Within the next several years, the wearable electronic and implantable medical devices market will reach \$31.2 billion and \$73.9 billion, respectively. Currently, the most commonly used power source is the rigid lithium ion battery. In order to further optimize the devices, flexible autonomous power sources, such as thermoelectric generators, can replace traditional battery systems.

Flexible thermoelectric films were created using a wet deposition approach and synthesized into ink suitable for either spin coating or screen printing. This study focuses on Seebeck coefficient, electrical conductivity, and thermal conductivity measurements.

Stable thermal and electrical contacts to measure the power factor of flexible films were achieved by decreasing thermocouple pressure and minimizing excess handling of the sample once it was mounted.  $\text{Cu}_2\text{Se}$  thin films annealed at  $430^\circ\text{C}$  exhibited the highest power factor of  $0.62 \text{ mW/mK}^2$  at  $411^\circ\text{C}$ . The highest power factor for  $\text{Bi}_2\text{Te}_{2.8}\text{Se}_{0.2}$  thick films annealed at  $430^\circ\text{C}$  was  $0.56 \text{ mW/mK}^2$  at  $186^\circ\text{C}$ . Due to excess heat conduction losses, thermal conductivity is the most difficult property to accurately measure for low thermal conductivity samples. The in-plane thermal conductivity was measured to be as low as  $0.39 \text{ W/mK}$  for a  $700\mu\text{m}$  thick  $\text{Bi}_2\text{Te}_{2.8}\text{Se}_{0.2}$  paste pellet. Measurement of all three thermoelectric properties opens up many opportunities to further improve material efficiency and begin device fabrication.

## TABLE OF CONTENTS

ACKNOWLEDGEMENTS .....	iv
ABSTRACT .....	v
LIST OF TABLES .....	ix
LIST OF FIGURES .....	x
LIST OF ABBREVIATIONS.....	xiii
CHAPTER 1: BACKGROUND .....	1
1.1 Overview of Power Harvesting Applications .....	1
1.1.1 Wearable Electronic Devices.....	1
1.1.2 Implantable Biomedical Devices .....	3
1.2 Existing Power Sources .....	4
1.2.1 Conventional Power Sources .....	4
1.2.2 Piezoelectric Power Source.....	6
1.2.3 Electromagnetic Power Source .....	7
1.2.4 Electrostatic Power Source .....	7
1.3 Overview of Thermoelectric Generators .....	8
1.3.1 Seebeck Effect .....	10
1.3.2 Figure of Merit.....	11
1.4 Characterization Methods for Thermoelectric Properties.....	12
1.4.1 Seebeck Coefficient .....	12

1.4.2 Electrical Conductivity .....	13
1.4.3 Thermal Conductivity .....	16
CHAPTER 2: THERMAL CONDUCTIVITY MEASUREMENT METHODS AND RESULTS.....	23
2.1 Experimental Methods of Thermal Conductivity .....	23
2.2 Results and Discussion of Thermal Conductivity.....	31
2.2.1 Measurement of Calibration Samples .....	31
2.2.2 Measurement of Bi <sub>2</sub> Te <sub>2.8</sub> Se <sub>0.2</sub> Paste Pellet.....	32
2.2.3 Measurement of Bi <sub>2</sub> Te <sub>2.8</sub> Se <sub>0.2</sub> Film .....	35
CHAPTER 3: SEEBECK COEFFICIENT AND ELECTRICAL CONDUCTIVITY MEASUREMENT OF THIN AND THICK FILMS.....	38
3.1 Experimental Methods of Seebeck Coefficient and Electrical Conductivity ..	38
3.2 Study of Bi <sub>2</sub> Te <sub>3</sub> and Cu <sub>2</sub> Se Spin Coated Thin Films .....	40
3.2.1 Material Synthesis.....	40
3.2.2 Experimental Results and Discussion on Spin Coated Thin Films...41	
3.4 Study of Bi <sub>2</sub> Te <sub>2.8</sub> Se <sub>0.2</sub> Screen Printed Thick Films .....	54
3.4.1 Material Synthesis.....	54
3.4.2 Experimental Results and Discussion of Screen Printed Thick Films .....	54
CHAPTER 4: CONCLUSIONS AND FUTURE WORK.....	62
4.1 Conclusions.....	62
4.1.1 Thermal Conductivity Measurement .....	62
4.1.2 Seebeck Coefficient and Electrical Conductivity Measurements .....	63
4.2 Future Work .....	64
4.2.1 Thermal Conductivity Measurement .....	64

4.2.2 Design of Thermoelectric Device .....	66
REFERENCES .....	67

## LIST OF TABLES

Table 1:	Calibration thermal conductivity samples .....	31
Table 2:	$\text{Bi}_2\text{Te}_{2.8}\text{Se}_{0.2}$ paste pellet thermal conductivity .....	35
Table 3:	Thermoelectric performance literature comparison.....	61

## LIST OF FIGURES

Figure 1:	Wearable electronic patch [2] .....	2
Figure 2:	A cantilever beam piezoelectric undergoing material deformation to generate a piezoelectric voltage [20] .....	6
Figure 3:	A cantilever electromagnetic generator converting mechanical vibrations into electrical power [23] .....	7
Figure 4:	Two types of electrostatic generators: (left) variable-capacitance-type capacitor and (right) variable-gap parallel-plate capacitor [19] .....	8
Figure 5:	Schematic of TEG [33] .....	10
Figure 6:	In-plane differential Seebeck measurement set-up .....	13
Figure 7:	Linear four point probe measurement set-up [39] .....	14
Figure 8:	Van der Pauw measurement set-up [39] .....	15
Figure 9:	Total thermal conductance measurement set-up .....	18
Figure 10:	Variable-linewidth $3\omega$ method .....	19
Figure 11:	Laser set-up for transient thermoreflectance method [52] .....	21
Figure 12:	Thermal conductivity experimental methods set-up .....	23
Figure 13:	Kapton sample holder scaled against a ruler with 1 mm gradations .....	24
Figure 14:	Teflon clamps for hot and cold side .....	25
Figure 15:	Schematic of hot and cold side Teflon clamps .....	26
Figure 16:	Baseline parallel thermal conductance set-up .....	27
Figure 17:	Thermocouples attached to kapton sample holder with silver paint .....	28
Figure 18:	Baseline parallel thermal conductance set-up .....	28

Figure 19:	An example of the linear relation between power from the heater and the temperature change in the sample .....	29
Figure 20:	Total parallel thermal conductance set-up .....	31
Figure 21:	Baseline and total thermal conductance of pellet A.....	33
Figure 22:	Baseline and total thermal conductance of pellet B.....	34
Figure 23:	Parallel thermal conductance set-up with $\text{Bi}_2\text{Te}_{2.8}\text{Se}_{0.2}$ film.....	36
Figure 24:	Revised parallel thermal conductance set-up with $\text{Bi}_2\text{Te}_{2.8}\text{Se}_{0.2}$ film.....	37
Figure 25:	LSR-3 Linseis - Seebeck coefficient & electric resistivity [image courtesy of Linseis website].....	38
Figure 26:	LSR measurement set-up [image courtesy of Linseis website] .....	39
Figure 27:	LSR thin film adapters .....	40
Figure 28:	Seebeck coefficient $\text{Bi}_2\text{Te}_3/\text{Al}_2\text{O}_3$ 350°C.....	41
Figure 29:	Electrical conductivity $\text{Bi}_2\text{Te}_3/\text{Al}_2\text{O}_3$ 350°C.....	42
Figure 30:	Thermocouple damage.....	43
Figure 31:	Schematic of graphite cover.....	43
Figure 32:	Seebeck coefficient $\text{Bi}_2\text{Te}_3/\text{Al}_2\text{O}_3$ 350°C graphite covers .....	44
Figure 33:	Electrical conductivity $\text{Bi}_2\text{Te}_3/\text{Al}_2\text{O}_3$ 350°C graphite covers .....	45
Figure 34:	Graphite cover adhering to sample surface.....	45
Figure 35:	Schematic of exaggerated graphite cover and sample contact.....	46
Figure 36:	a) before and b) after liquid graphite deposition (red circles indicate thermocouple placement).....	46
Figure 37:	Corrected distance.....	47
Figure 38:	Seebeck coefficient $\text{Cu}_2\text{Se}/\text{Al}_2\text{O}_3$ graphite stencil .....	48
Figure 39:	Electrical conductivity $\text{Cu}_2\text{Se}/\text{Al}_2\text{O}_3$ graphite stencil .....	49
Figure 40:	Seebeck coefficient showing repeatability.....	50

Figure 41:	Electrical conductivity showing repeatability.....	51
Figure 42:	Electrical conductivity of $\text{Cu}_2\text{Se}/\text{Al}_2\text{O}_3$ at various annealing temperatures .....	52
Figure 43:	Seebeck coefficient of $\text{Cu}_2\text{Se}/\text{Al}_2\text{O}_3$ at various annealing temperatures .....	53
Figure 44:	Power factor of $\text{Cu}_2\text{Se}/\text{Al}_2\text{O}_3$ at various annealing temperatures .....	53
Figure 45:	Seebeck coefficient of $\text{Bi}_2\text{Te}_{2.8}\text{Se}_{0.2}$ at various annealing temperatures ...	56
Figure 46:	Electrical conductivity of $\text{Bi}_2\text{Te}_{2.8}\text{Se}_{0.2}$ at various annealing temperatures .....	56
Figure 47:	Power factor of $\text{Bi}_2\text{Te}_{2.8}\text{Se}_{0.2}$ at various annealing temperatures.....	57
Figure 48:	Seebeck coefficient of $\text{Bi}_2\text{Te}_{2.8}\text{Se}_{0.2}$ annealed at $430^\circ\text{C}$ for various annealing durations .....	58
Figure 49:	Electrical conductivity of $\text{Bi}_2\text{Te}_{2.8}\text{Se}_{0.2}$ annealed at $430^\circ\text{C}$ for various annealing durations .....	58
Figure 50:	Power factor of $\text{Bi}_2\text{Te}_{2.8}\text{Se}_{0.2}$ annealed at $430^\circ\text{C}$ for various annealing durations.....	59
Figure 51:	Temperature-dependent (a) Electrical conductivity (b) Seebeck coefficient (c) Thermal conductivity and (d) ZT of a control pellet and flexible film.....	60

## LIST OF ABBREVIATIONS

LFA	Laser Flash Apparatus
LSR	LSR-3 Linseis – Seebeck coefficient & electric resistivity
TE	Thermoelectric
TEG	Thermoelectric generator
PTC	Parallel thermal conductance

## CHAPTER 1: BACKGROUND

### **1.1 Overview of Power Harvesting Applications**

#### 1.1.1 Wearable Electronic Devices

The market for wearable electronic devices is quickly growing [1]. According to a Markets and Markets report, it is estimated that by the year 2020, the overall wearable electronic market will reach \$31.2 billion. Many of these wearable devices are used for preventative healthcare in order to monitor physiological signals and transmit data wirelessly. This allows health professionals to receive data and monitor the health of their patients for both critical and non-critical applications. Non-invasive physiological data that can be measured includes electrocardiograms, blood pressure, heart rate, oxygen saturation, skin temperature, sweat production, and motion [2-4]. In order to collect these physiological signals, electrical, optical, mechanical, and chemical measurements must be recorded.

The comfort and power consumption of 24/7 wearable devices must be considered. The size of the wearable device should be as small as possible and follow the contours of the body shape in order to limit any physical or visual distractions. As can be seen in Figure 1, this wearable electronic patch uses a rigid lithium ion battery as the device's power source. However, the lithium ion battery must be charged once a week in order to run continuously [2]. Although these traditional batteries improve the lifetime of the device, they also make the device much more bulky and uncomfortable.

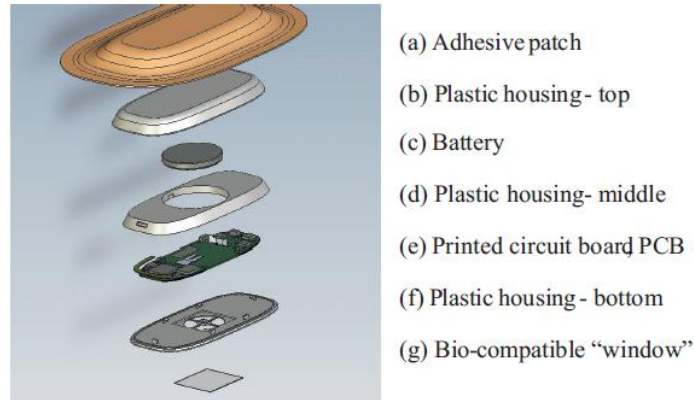


**Figure 1: Wearable electronic patch [2]**

In addition, energy and power should be considered for these devices. Energy is the total quantity of work supplied to the device. The total amount of energy required for a particular wearable device will always be the same, regardless of the power source that is selected. However, the power supplied to the device can change. Since power is the rate of energy produced, various power sources may provide more or less power. However, all power sources will ultimately supply the same amount of energy to the device. If a device requires intermittent data transmission, the power requirement will be lower than a device that requires continuous data transmission.

Improvement of wearable electronic devices involves optimization of the sensors as a way to decrease the amount of required power. Minimizing the use of general radio communication can drastically improve power consumption. Therefore, when measuring a non-critical signal, data should only be transmitted when a critical condition is reached [2]. Ultimately, further improvement of the design size and shape requires a flexible, autonomous power source that can provide adequate power without constant maintenance.

### 1.1.2 Implantable Biomedical Devices

In addition to wearable devices, many implantable devices such as pacemakers, cardiac defibrillators, and neurological stimulators continue to become smaller, more efficient, and robust. As the field of implantable medical devices continues to grow, more and more people are beginning to receive these devices. By the year 2018, it is predicted that the U.S. market for implantable medical devices will be \$73.9 billion, according to a Transparency Market Research report.

#### 1.1.2.1 Neurological Stimulators

Neurological stimulators are devices designed to send electrical stimulations to specific regions of the brain. These devices are oftentimes used to help provide therapeutic benefits for Parkinson's disease, essential tremors, or obsessive-compulsive disorder. Currently, the lifespan of a neurological stimulator power source used to treat movement disorders is 5 years [5]. For the treatment of other symptoms, such as obsessive-compulsive disorder, the power requirement can be much higher and range from 1mW-100mW [6]. As a result, this increased power requirement reduces the power source's overall life span. Rechargeable power sources for neurological stimulators are also an option, which allows the lifespan of the battery to reach the order of 10 to 15 years [7]. According to the World Health Organization, an estimated 7 to 10 million people worldwide are living with Parkinson's disease. Meanwhile, the neurological market is projected to hit \$5 billion by 2020 according to an iData Research Report.

#### 1.1.2.2 Pacemakers and Cardiac Defibrillators

Pacemakers are similar to neurological stimulators, in that they supply electrical impulses to the heart muscles in order to aid in abnormal heart beats. Some pacemaker

devices also include a cardiac defibrillator. The purpose of an implantable cardiac defibrillator is to deliver an amount of electrical energy to the heart, allowing the heart to resume the normal heart beat rhythm. Over the years, the power requirement for pacemakers has been significantly reduced and can range from  $1 \mu\text{W}$ - $8 \mu\text{W}$  [8, 9]. In addition, the energy cost is approximately  $0.5$ - $1.2 \mu\text{J}$  depending on the pacing output demands [10]. The estimated forecast for the cardiac pacemakers market is \$5.7 billion by 2016 according to Research and Markets. In fact, North America will account for approximately 40% of the global market.

The continuous and intermittent power requirements for implantable medical devices continue to decrease as our technology advances [11]. In addition, both the neurological stimulator and pacemaker markets are expected to increase. This could possibly be due to the increasing amount of elderly citizens requiring implantable medical devices. It is projected that the population of the world over 65 years of age will increase from 6.8% to 16.2% as the baby boomer demographic begins to approach retirement age [12]. The continual improvement in implantable medical devices has shown that power requirements are in the  $\mu\text{W}$  range [9, 13-15].

## **1.2 Existing Power Sources**

### **1.2.1 Conventional Power Sources**

Currently, both wearable and implantable medical devices utilize conventional batteries such as lithium cells. However, these power sources are unable to outlast the lifespan of the medical device. As a result, these power sources require a form of either replacement or recharging.

Many wearable devices require frequent charging. In addition, the overall thickness of rigid lithium batteries makes them difficult to wear without being physically or visually annoying. As a result, current devices require placement in a location that won't hinder the ability to perform daily activities. Therefore, many of these devices are being placed underneath clothing.

For an implantable device such as a cardiac defibrillator, the average lifespan for a patient is 10 years whereas the device itself is only able to function for 4.7 years [16]. Ultimately, the difference between the power source and service life of the device affects the patient. When the service life of the device ends, the patient needs to undergo surgical replacement. Aside from being a significant physical and emotional burden, there is also an economic burden. However, conventional power sources, such as lithium ion cells continue to be the most reliable source available on the market.

Lithium cells remain the main power source in wearable and implantable medical devices due to their energy density of  $2880 \text{ J/cm}^3$  and reliability [17]. The lithium batteries selected for medical applications exhibit a change in discharge voltage as the remaining energy reduces. This allows for enough time for the power source to either be recharged or replaced before complete failure of the medical device. In addition, lithium batteries use a solid electrolyte for producing power, resulting in minimal battery leakage compared to alternative liquid batteries [16]. Although lithium cells have proven to be the mainstay for now, other power sources have been implemented experimentally such as nuclear batteries and bio-fuel cells.

Ultimately, it is the goal for thermoelectric devices to harvest waste body heat for use in powering medical devices. Alternative energy harvesting solutions that may be

used to power medical devices include piezoelectric, electromagnetic, or electrostatic power sources. However, directly comparing the performance of lithium ion cells to alternative power sources can be difficult. Typically, the energy density of lithium cells are used for comparison, while the power density is used to compare alternative power sources [17].

### 1.2.2 Piezoelectric Power Source

The piezoelectric effect occurs when the material undergoes a mechanical strain. As can be seen in Figure 2, an electrical voltage is created that is proportional to the mechanical strain. Utilizing this piezoelectric effect can result in converting mechanical motion to electrical energy. Roundy *et al.* demonstrated that a piezoelectric power source of  $1 \text{ cm}^3$  can produce  $200 \text{ } \mu\text{W}$  [17]. However, use of a piezoelectric power source does have its drawbacks. This potential energy source can only be adhered or implanted in high force regions of the body, such as knees, hips, or ankles. The placement of this power source determines how much power is produced. If the piezoelectric generator is not placed in a high force or frequently moving portion of the body, electrical energy will not be produced [18]. Thus, the power generated using piezoelectrics as a power source are dependent on the mobility of the individual [19].

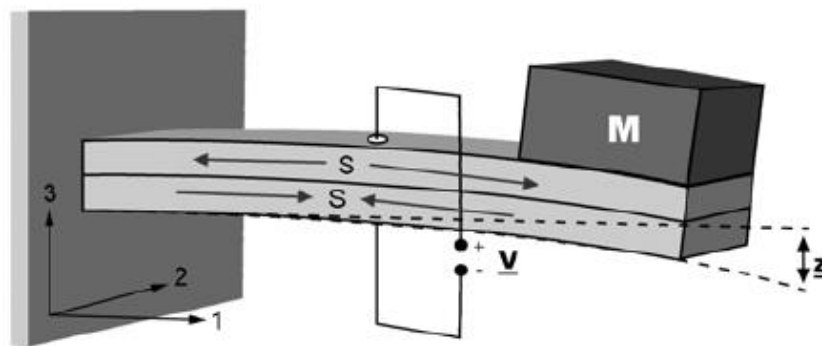


**Figure 2: A cantilever beam piezoelectric undergoing material deformation to generate a piezoelectric voltage [20]**

### 1.2.3 Electromagnetic Power Source

Electromagnetic generators generally consist of a coil of tightly wrapped wires. When this coil moves through a magnetic field, a voltage is generated. The amount of voltage generated is dependent on the strength of the magnetic flux between the coil and magnetic field. This method of converting mechanical vibrations between a coil and magnet to produce electrical energy is based on the magnetic induction principle [6, 21]. Electromagnetic power sources are capable of producing  $46 \mu\text{W}$ , which results in a power density of  $307 \mu\text{W}/\text{m}^3$  [22]. There are several types of designs, but in each case, either the magnet or coil moves relative to the other. Figure 3 illustrates a cantilever type generator.

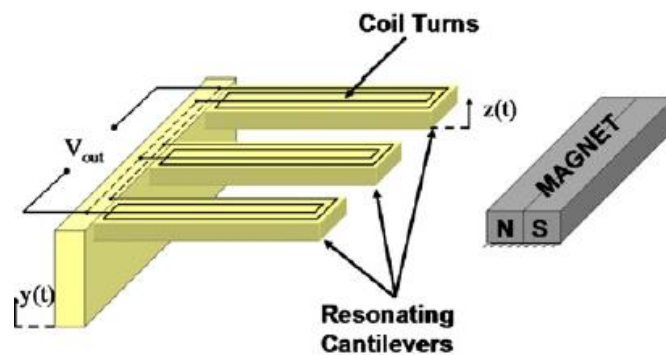


**Figure 3: A cantilever electromagnetic generator converting mechanical vibrations into electrical power [23]**

### 1.2.4 Electrostatic Power Source

Electrostatic generators convert mechanical vibrations into electrical energy as the transducer moves against the electrical field. Harvesting energy from electrostatic generators is dependent on the charging of the capacitor plates. Vibrations or any other motion separates the plates of the charged capacitor, resulting in a change in voltage across the capacitor. The newly created voltage can then be used for various applications. Theoretical results indicate that a power density of  $58 \mu\text{W}/\text{cm}^3$  is achievable [24]. As can

be seen in Figure 4, the mechanical energy input to the system is converted into electrical energy [19, 25].

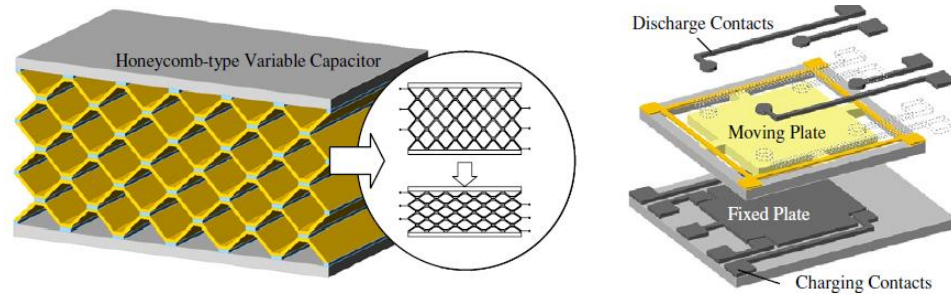


**Figure 4: Two types of electrostatic generators: (left) variable-capacitance-type capacitor and (right) variable-gap parallel-plate capacitor [19]**

In the case for these power sources, continual mechanical vibrations are required to create a steady source of electrical energy. Therefore, when the patient stops moving, the generator required to power their medical device is no longer working. As a solution, capacitors are being incorporated to help provide a permanent supply of electrical energy to these medical devices [21, 26].

Power sources that can provide a continual supply of energy without the need for human movement allows for an increased variety of placement on the human body. In addition, power sources that are independent of human movement can be used for patients with limited mobility. Development of a thermoelectric generator that can produce power in the  $\mu\text{W}$  range would advance both the energy harvesting and medical field.

### 1.3 Overview of Thermoelectric Generators

Thermoelectric materials are an ideal energy harvester choice due to their ability to generate sufficient power without the need for mechanical vibrations. In order to use piezoelectric, electromagnetic, and electrostatic energy harvesters for implantable

medical devices, some form of human movement or exertion of a force to generate electrical energy is required. In addition, these alternative energy sources consist of a rigid design, making them difficult to implement in many medical devices.

Thermoelectric generators (TEGs), however, are an alternative energy source that has recently gained interest as a potential medical device power solution. TEGs have the ability to produce power in the  $\mu\text{W}$ - $\text{mW}$  range, making them an ideal solution for wearable and implantable medical devices [8, 9]. When a person has a lower metabolic rate, a TEG has been shown to produce 100-150  $\mu\text{W}$ . However, with an increase in physical activity, the TEG can produce 500-700  $\mu\text{W}$  [27]. Since TEGs operate using the Seebeck effect, only a temperature gradient is required to produce power. In addition, fabrication of flexible TEGs allow for these devices to be applied to irregularly shaped surfaces [28].

The highest temperature gradient within the human body is closest to the skin surface. For wearable devices, the temperature gradient is created between the hot temperature of the skin and the relatively cold room temperature. Implantable biomedical devices utilize the temperature gradient created between the body core and skin surface. The temperature gradient for an implantable medical device can reach  $3.5^{\circ}\text{C}$ , depending on the physical activity of the person [15]. As for wearable sensors, it is possible to achieve temperature gradients greater than  $10^{\circ}\text{C}$ . Since there is a larger temperature gradient for wearable sensors, the potential for thermoelectric energy harvesting will be greater than for implantable devices.

### 1.3.1 Seebeck Effect

The Seebeck effect transforms thermal energy into electrical energy. When a temperature gradient is applied across a semiconductor or conductor material, a voltage is generated, often referred to as the Seebeck voltage [29-32]. As shown in Figure 5, two materials, such as a metal and semiconductor, form junctions to create a TEG. The junction refers to the connection made between a high electrically conductive metal, such as silver, and the thermoelectric materials. This allows the thermoelectric materials to be connected electrically in series and thermally in parallel. By placing the thermoelectric materials in parallel, the Seebeck effect can be utilized. The Seebeck effect occurs when the electrical charge carriers travel from the hot side to the cold side. As a result of the increased thermal energy at the hot side, the charge carrier energy increases while the charge carrier energy at the cold side decreases. In order to reach equilibrium, the charge carriers diffuse from the hot side to the cold side. Therefore, a potential difference is created. This electrochemical potential, the Seebeck voltage, occurs as a result of the thermal gradient. When a small temperature gradient is applied, the Seebeck voltage is directly proportional to the temperature difference.

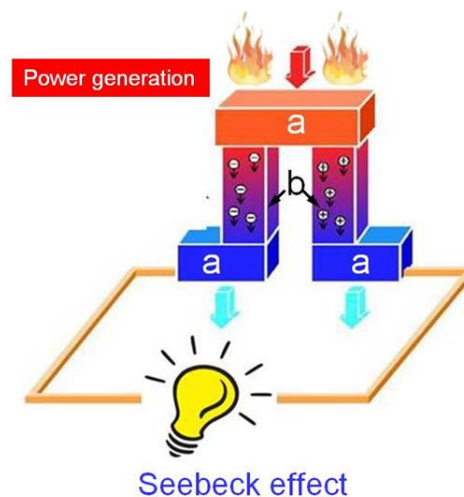


**Figure 5: Schematic of TEG [33]**

The Peltier effect produces a temperature gradient when a voltage is applied across the material. This is the inverse process to the Seebeck effect.

### 1.3.2 Figure of Merit

In order to compare the efficiency of thermoelectric material properties, the dimensionless figure of merit (Equation 1-1) is used.

$$ZT = \frac{\alpha^2 \sigma}{\kappa} T \quad [1-1]$$

where  $\alpha$ ,  $\sigma$ ,  $\kappa$ , and  $T$  are the Seebeck coefficient, electrical conductivity, thermal conductivity, and absolute temperature, respectively [34, 35]. Many research studies focus on the measurement of the power factor,  $\alpha^2 \sigma$ . This is mainly due to the difficulty in obtaining an accurate thermal conductivity measurement for thin film thermoelectric materials.

The figure of merit is an important equation since this provides a way to compare the material's overall thermoelectric properties. It is desired to maximize the figure of merit since this indicates the material's ability to efficiently produce thermoelectric power. If a material with poor thermoelectric properties is selected, the thermoelectric generator will also exhibit poor properties. In order to maximize the figure of merit, the Seebeck coefficient and electrical conductivity must be large while a low thermal conductivity is maintained [36]. A low thermal conductivity is necessary in order to maintain a large temperature gradient and minimize heat flow from the hot and cold side. The electrical conductivity must be high in order to efficiently conduct electrical current. In addition, Joule heating must be minimized, which can affect the thermal conductivity. A material with a large Seebeck coefficient will generate a large Seebeck voltage when a temperature gradient is present.

However, maximizing the electrical conductivity and the Seebeck coefficient while minimizing thermal conductivity proves to be difficult. These material properties are a result of the material's electronic structure and scattering of charge carriers, making it difficult to isolate and independently control one property [37].

## **1.4 Characterization Methods for Thermoelectric Properties**

### 1.4.1 Seebeck Coefficient

The Seebeck coefficient is the only thermoelectric property that is independent of sample dimension. As show in equation 1-2, the Seebeck coefficient measurement requires a temperature gradient to be applied to the sample in order to measure the induced voltage.

$$S = -\frac{V}{\Delta T} \quad [1-2]$$

where  $V$  and  $\Delta T$  are the voltage induced by the sample and the temperature difference between two points, respectively.

The in-plane Seebeck measurement requires the temperature gradient to be applied across the surface of the sample. This can be achieved by suspending the sample across two isothermal blocks, as shown in Figure 6. The heat sink is typically a large copper block while the heat source is a strain gage or cartridge heater [38, 39]. This allows the sample to maintain a steady temperature gradient. The sample then generates a voltage that is measured using two electrical probes. In addition, thermocouples are placed at the same location as the electrical probes to determine the magnitude of the temperature difference. N-type materials will exhibit a negative Seebeck coefficient while a p-type material will have a positive Seebeck coefficient.

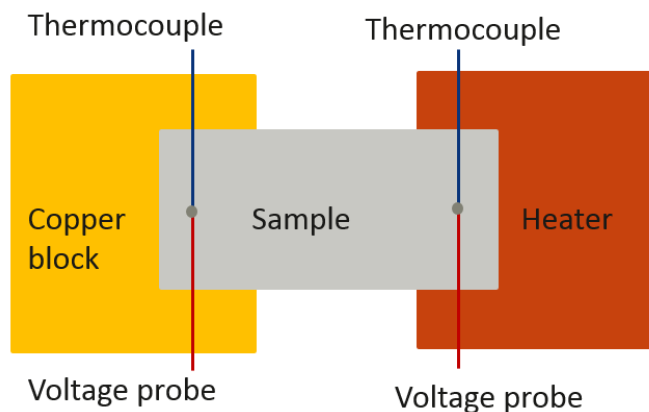


**Figure 6: In-plane differential Seebeck measurement set-up**

The differential method is the most common Seebeck coefficient measurement method. The differential method applies small thermal gradients along the sample. Multiple data points with varying temperature differences are collected. The linear slope of the voltage with respect to the temperature gradient produces the Seebeck coefficient. In order to achieve an accurate and high linearity, it is important to determine an adequate wait time to achieve thermal equilibrium. Obtaining a good thermal contact is also necessary to achieve accurate results. For many thin and thick films, it is difficult to obtain a good thermal contact without damaging the film surface.

#### 1.4.2 Electrical Conductivity

Various methods have been developed to characterize the electrical conductivity of thin and thick film materials. This section focuses on two main measurement methods used.

##### Linear Four-Point Probe Method

The most common characterization method to determine the electrical conductivity of thin or thick film is the linear four-point probe method [39]. This method applies a constant current source to the two outer electrodes while measuring the floating

potential along the two inner electrodes. Figure 7 shows the configuration of the collinear four-point probes equally spaced on the sample surface.

If the film sample size is larger than the probe spacing and the film thickness is less than half the probe spacing, the electrical conductivity formula for collinear four-point probes with equal spacing becomes:

$$\sigma = \frac{\ln 2}{\pi d} \frac{I}{V} \quad [1-3]$$

where  $d$ ,  $I$ , and  $V$  are the probe spacing distance, current, and voltage, respectively [39, 40]. This formula is based on the sample geometry and probe spacing.

Some other constraints that must be taken into consideration are the diameter of the probe, boundaries, and film thickness. In relation to the probe distance, the diameter of the probe must be small. In addition, the boundary between the probes and sample surface should be small and hemispherical. Meanwhile, for certain film thicknesses and small sample sizes, a correction factor must be applied [41-43].

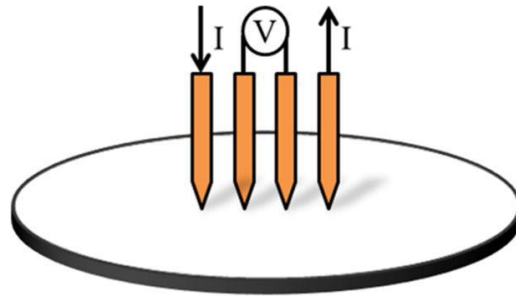


**Figure 7: Linear four point probe measurement set-up [39]**

#### Van der Pauw Method

For film samples of arbitrary shape, the van der Pauw method is an alternate electrical conductivity measurement [39]. Although the probe placement shown in Figure

8 is on the corners, samples of arbitrary shape require the probes to be placed along the perimeter of the sample.

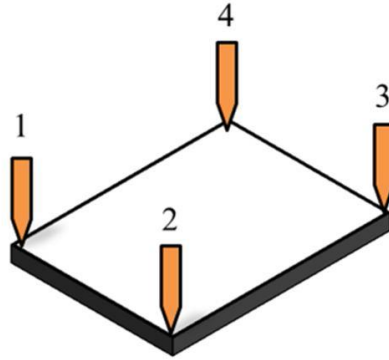


**Figure 8: Van der Pauw measurement set-up [39]**

To achieve accurate results, it is important to obtain a good electrical contact. This can be achieved by placing a small amount of indium to the tip of each probe. Alternatively, metal contacts can be deposited by sputtering deposition. However, the size of the contacts must be smaller than the sample size, the sample quality must be homogenous, and the sample thickness must be uniform in order for the van der Pauw method to be applicable [44].

The van der Pauw method consists of two resistance measurements [45]. During the first measurement, a constant current is applied between probes 1 and 2 (Figure 8). Meanwhile, the voltage is measured between probes 3 and 4. This first resistance is calculated using Ohm's law:  $R_{12,34} = V_{34}/I_{12}$ . The second resistance measurement repeats the previously discussed process where constant current is applied between probes 2 and 3 while the voltage is measured between probes 1 and 4. Once these two resistance measurements are completed, the sample sheet resistance  $R_s$  is calculated with equation 1-4.

$$e^{-\pi \cdot R_{12,34}/R_s} + e^{-\pi \cdot R_{23,14}/R_s} = 1 \quad [1-4]$$

where  $R_{12,34}$  is the resistance measured when current is passed through probes 1 and 2 and voltage is measured through probes 3 and 4.

Once the sheet resistance is calculated, the in-plane electrical conductivity of the thin film sample can then be calculated using equation 1-5.

$$\sigma = \frac{1}{(R_s \cdot L)} \quad [1-5]$$

where  $L$  is the sample thickness and  $R_s$  is the sample sheet resistance.

### 1.4.3 Thermal Conductivity

Thermal conductivity is the most difficult property to accurately determine. Oftentimes, the thermoelectric material's power factor is reported since measurement of the thermal conductivity has proven to be complex. Typically, there are many losses that must be accounted for such as convection, radiation, power losses, and thermal contacts. In addition, many in-plane measurement methods require thicker films, no substrates, or high in-plane thermal conductivity, which are not always feasible options. In this section, several thermal conductivity measurement methods for thin films are discussed.

#### 1.4.3.1 Steady-State Method

The steady-state method involves the measurement of the thermal resistance of the sample. This is achieved by measuring the temperature difference across the sample due to a temperature gradient supplied by a powered heater. Equation 1-6 shows the calculation for the thermal conductivity  $k$  of the sample.

$$k = \frac{P}{\Delta T} \cdot \frac{L}{A} \quad [1-6]$$

where  $P$ ,  $\Delta T$ ,  $L$ , and  $A$  are the power supplied to the heater, temperature difference, length between the thermocouples, and cross-sectional area of the sample.

The principal difficulty associated with this method is the accurate determination of the power going through the sample. Due to many power losses such as radiation, heat conduction, and convection, the power input does not equal the power through the sample. Performing the experiments in a vacuum chamber with a radiation shield helps to reduce the convection and radiation losses. However, it is extremely difficult to completely eliminate all heat losses. Typically, the measurement of calibration samples are used to account for the total heat losses.

#### 1.4.3.2 Parallel Thermal Conductance Method

One method that is a variation of the steady state technique is the parallel thermal conductance method [46, 47]. In order to avoid convection and radiation losses, the measurement is performed in a cryostat vacuum chamber with a radiation shield placed around the sample. Supplying power to a strain gage heater creates the temperature gradient.

The distance between the thermocouples is predetermined with a plastic sample holder. This low thermal conductivity sample holder initially supports the strain gage heater and thermocouples. A baseline thermal conductance measurement is first taken in order to account for all background thermal conduction losses. The thermal conductance of the sample holder is calculated using equation 1-7.

$$c = \frac{I^2 R}{\Delta T} \quad [1-7]$$

where  $I$ ,  $R$ , and  $\Delta T$  are the current supplied to the heater, the resistance of the heater, and the temperature difference between the two thermocouples. The sample is then attached with silver paste to form a good thermal contact. The total thermal conductance of the system is then measured (Figure 9).

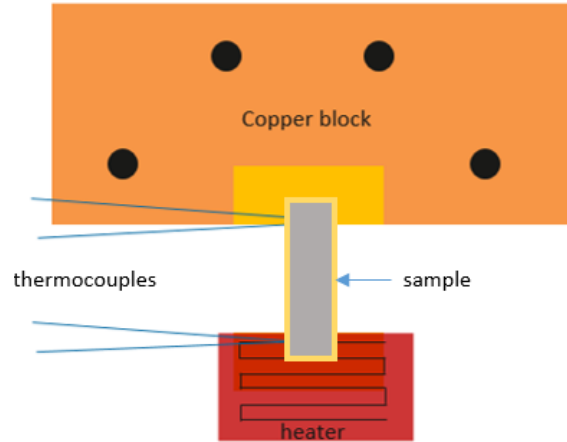


**Figure 9: Total thermal conductance measurement set-up**

In order to determine the thermal conductance of just the sample, the baseline thermal conductance is subtracted from the total thermal conductance. Entering the sample's cross-sectional area and the length between the two thermocouples, equation 1-8 can be used to determine the in-plane thermal conductivity of the sample.

$$k = (C_{total} - C_{baseline}) \cdot \frac{L}{A} \quad [1-8]$$

where  $C_{total}$ ,  $C_{baseline}$ ,  $L$ , and  $A$  are the total thermal conductance, baseline thermal conductance, distance between the thermocouples, and sample cross-sectional area, respectively.

Due to the simple sample preparation and measurement set-up requirements, the parallel thermal conductance method is a desired method to try initially. However, it can be more difficult to accurately measure supported films due to heat loss through the substrate. In addition, the difficulties discussed for the steady-state method also apply to the parallel thermal conductance method.

#### 1.4.3.3 Variable-linewidth $3\omega$

Oftentimes, it can be difficult to measure suspended films. Therefore, the variable-linewidth  $3\omega$  method can be used for measuring supported films [48, 49]. For

this method, one wide thin metallic  $3\omega$  heater and one narrow thin metallic  $3\omega$  heater are deposited onto the sample surface (Figure 10). Based on the temperature-dependent change in electrical resistance, the metal heaters will also be used as a temperature sensor. The narrow heater will create a thermal resistance that is sensitive to the in-plane ( $k_x$ ) thermal conductivity while the much wider heater provides a uniform distribution of heat through the cross-plane ( $k_z$ ) thermal conductivity.

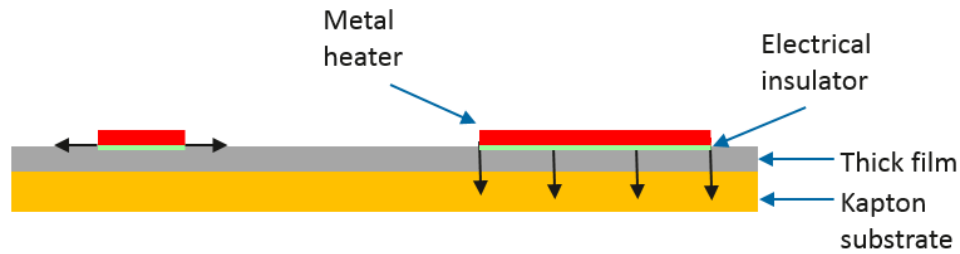


**Figure 10: Variable-linewidth  $3\omega$  method**

The traditional cross-plane  $3\omega$  method is used to measure the thermal conductivity of both the narrow and wide heater. An AC current with an angular modulation frequency  $\omega$  is first passed through the heater strip. As a result, a heating power and temperature oscillation with an angular frequency of  $2\omega$  is generated within the sample. Based on the temperature coefficient of electrical resistance of the heater, the temperature oscillation results in a change of the heater resistance with an angular frequency of  $2\omega$ . After determination of the current and heater resistance, the voltage with a frequency of  $3\omega$  can be calculated [50, 51]. As a result, the temperature response of the heater is measured with equation 1-9.

$$T_{2\omega} = \frac{2V_{3\omega}}{TCR \cdot V_{1\omega}} \quad [1-9]$$

where  $V_{3\omega}$ , TCR, and  $V_{1\omega}$  is the  $3\omega$  voltage, temperature coefficient of electrical resistance, and the amplitude of the voltage applied across the heater, respectively. In order to accurately measure the temperature of the sample, a calibration is performed to determine the temperature coefficient of electrical resistance.

Although this method is a more complicated measurement set-up than the parallel thermal conductance method, the variable-linewidth  $3\omega$  heating region can be better confined, resulting in less radiation losses. However, due to heat losses through the substrate, the variable-linewidth  $3\omega$  in-plane thermal conductivity is less sensitive than alternate suspended methods.

#### 1.4.3.4 Transient Thermorefectance

In order to measure the cross-plane thermal conductivity using a transient method, an optical approach is ideal. For the transient thermorefectance method, a laser system is used that sends a known laser pulse to heat the sample. Short optical heating pulses, which have a diameter of approximately  $20\ \mu\text{m}$ , only pulse for a few picoseconds, which allows the heat to travel a minimum depth of  $20\ \text{nm}$ . This shallow depth prevents any substrate effects and lateral spreading. The power of the laser is known and the change in surface temperature is monitored with a probing laser. To increase the signal-to-noise ratio, the reflected laser is displayed onto a two-channel fast photodiode. Figure 11 shows the transient thermorefectance measurement set-up.

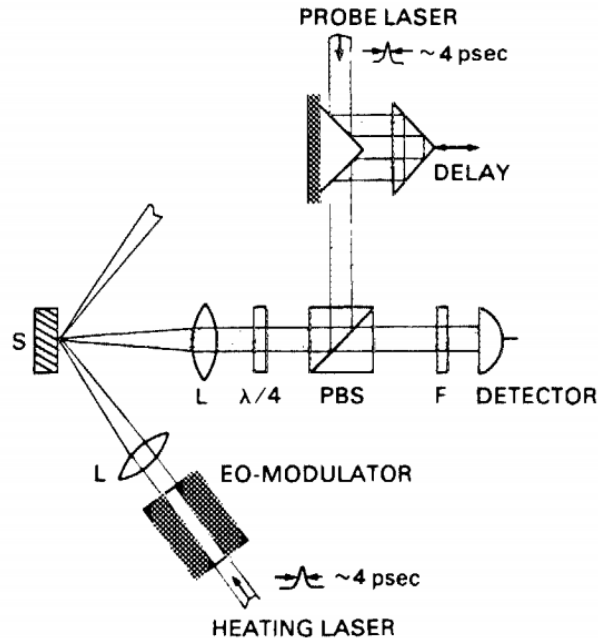


**Figure 11: Laser set-up for transient thermorefectance method [52]**

In order to probe the temperature response, the temperature dependence of the reflectivity is calculated using equation 1-10.

$$\frac{1}{r} \frac{dr}{dT} \quad [1-10]$$

where  $r$  and  $T$  are the reflectivity and temperature of the sample surface, respectively. Typically,  $10^{-7}$  is the limit of systems [52, 53]. To improve surface heating, a metal coating is applied to the sample.

Although this measurement method is ideal for measurement of the cross-plane thermal conductivity, accurately measuring the in-plane thermal conductivity with this method is more difficult.

Currently, it is difficult to measure the thermal conductivity of thick and thin films. As a result, the power factor of flexible films are usually published rather than the figure of merit. However, obtaining repeatable results for the power factor of flexible films can become increasingly more complicated due to the decreased sample thickness.

As a result, the thermocouples can easily scratch and damage the film surface. Therefore, the goal of this study is to be able to measure the Seebeck coefficient, electrical conductivity, and thermal conductivity of thick and thin films.

## CHAPTER 2: THERMAL CONDUCTIVITY MEASUREMENT METHODS AND RESULTS

### 2.1 Experimental Methods of Thermal Conductivity

The experimental methods to determine the in-plane thermal conductivity of thin and thick films utilizes the parallel thermal conductance method. This method was selected based on the straight forward measurement set-up. Since the parallel thermal conductance method uses a strain gage heater and thermocouples, no clean room fabrication processes were required. The overall process to measure the in-plane thermal conductivity of these films involves two measurements to determine the background losses and total thermal conductance (Figure 12). Since the parallel thermal conductance method is a variation of the steady-state method, it is assumed that there are no changes in the background losses when a sample is added to the set-up.

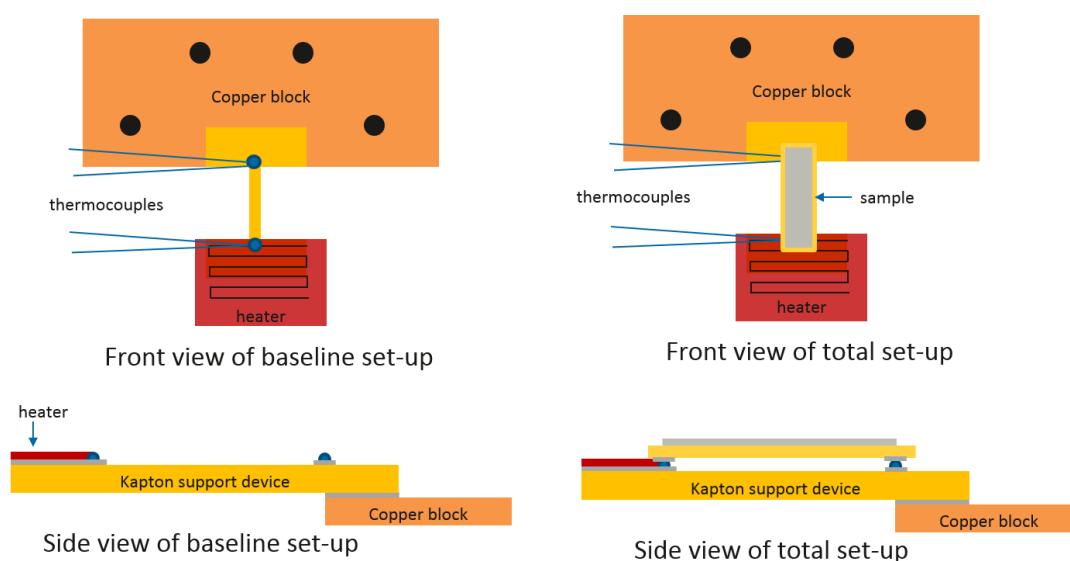


**Figure 12: Thermal conductivity experimental methods set-up**

The first measurement, referred to as the baseline, determines the background thermal conduction losses. Kapton is used as the sample holder due to a low thermal conductivity, which minimizes the baseline's thermal conductance. In addition, attaching the thermocouples to the kapton sample holder allows the thermocouples to remain at a fixed distance. Figure 13 shows a kapton sample holder with optimized dimensions by minimizing the length and width of the device. In order to create such a small design, Coreldraw 12 and a Universal Systems CNC laser system were used to create the kapton sample holder pattern. This process allowed for multiple kapton sample holders to be reliably produced with similar dimensions. The wider ends of the kapton allowed a heat source to be attached to one end of the holder while the other end was mounted to the cold sink. The width of the narrow mid-section was determined through trial-and-error in order to develop a wide enough mid-section to prevent breakage while preventing excess heat from traveling between the hot and cold side.

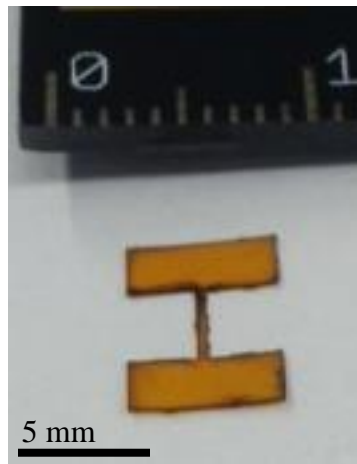


**Figure 13: Kapton sample holder scaled against a ruler with 1 mm gradations**

A 7.0 x 3.5 mm Omega linear strain gage heater with a resistance of 350 $\Omega$  was attached to one end of the kapton sample holder using SPI Flash Dry Silver Paint. The

silver paint maximized the heat transferred from the linear strain gage heater to the kapton sample holder while also forming a sufficient bond. The linear strain gage heater remained attached to the kapton sample holder during both the baseline and total thermal conductance measurements.

Initially, Teflon clamps were designed and machined for 0.03” diameter E-type Omega thermocouples. Teflon was chosen due to the low thermal conductivity properties that helped prevent excess heat transfer from the sample to the clamp. The thermocouples were placed and secured in the Teflon clamps. The cold side Teflon clamp/thermocouple was mounted on the cryostat stage using the pre-existing screw holes, as can be seen in Figure 14. This design allowed the Teflon clamp/thermocouple to sandwich the sample and kapton sample holder against the cryostat stage while applying enough pressure to get an accurate temperature reading. For the hot side Teflon clamp/thermocouple, two pieces of Teflon sandwiched the sample and kapton sample holder together.

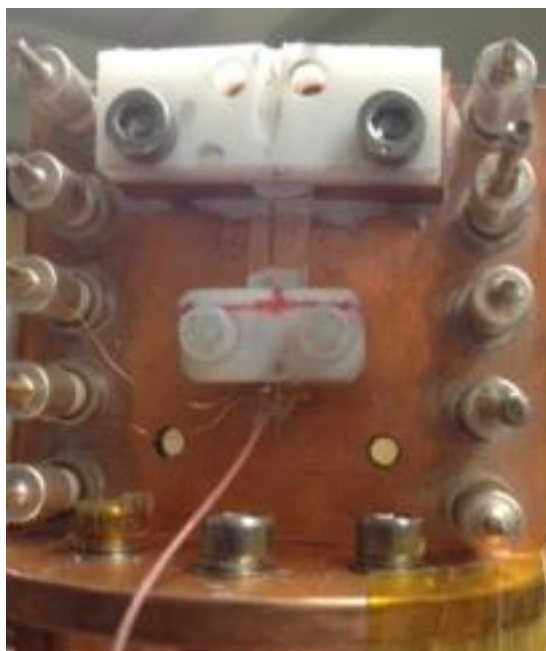


**Figure 14: Teflon clamps for hot and cold side**

A layer of Lydall LyTherm insulation was also attached to the cryostat stage in order to prevent the hot side Teflon clamp from directly touching the heat sink (Figure 15). By preventing direct contact between the hot side Teflon clamp and cryostat stage, additional heat conduction losses were minimized. In order to confirm the accuracy of this measurement set-up, a calibration alumina sample was measured. The experimentally measured thermal conductivity was 24.05 W/mK, whereas the reference value for alumina is reported to be 24.7 W/mK. The potential source of error between the reference and experimental values for alumina could be related to either the accuracy in the thermocouple's temperature reading or the accuracy in measuring the power supplied to the heater.

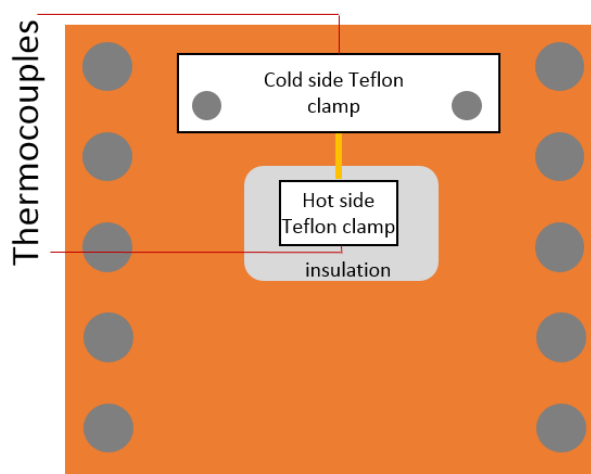


**Figure 15: Schematic of hot and cold side Teflon clamps**

However, when trying to measure a calibration sample with a much smaller thermal conductivity, such as a glass slide, this set-up was no longer sensitive enough to accurately measure the thermal conductivity. Further evaluation of the set-up led to the prediction that the thermocouple diameter was much too large to measure samples with a thermal conductivity closer to 0.5-1 W/mK. Instead, if a smaller thermocouple diameter

was used, the excess heat conduction losses could potentially be further minimized and a more accurate temperature reading could be obtained. Therefore, thermocouples were replaced with 0.003” diameter thermocouples, the Teflon clamps were replaced with silver paint, and the insulation attached to the cryostat stage was completely removed.

In the updated measurement set-up, the cold side kapton sample holder was attached to a removable copper block with silver paint. The removable copper block provided ease of sample mounting away from the cryostat stage. The cold side thermocouple (TC1) was attached at the edge of the copper block where the wide end and narrow support mid-section meet. Figure 16 shows a schematic of the entire baseline parallel thermal conductance set-up that was placed on the cryostat stage.

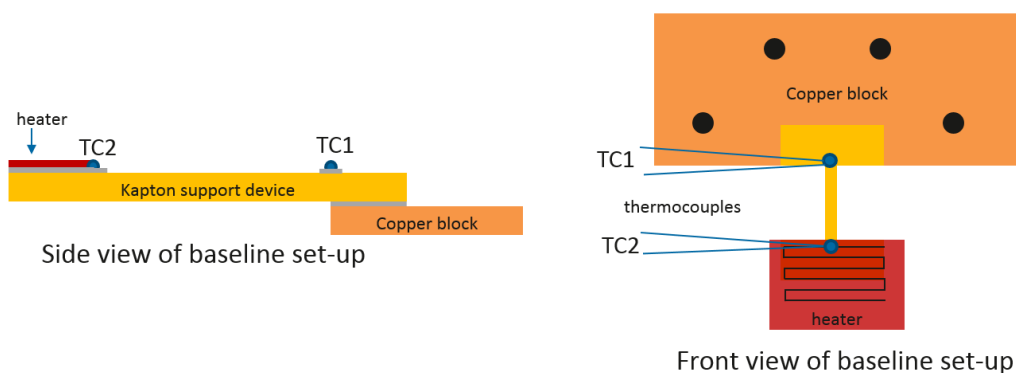


**Figure 16: Baseline parallel thermal conductance set-up**

E-type Omega thermocouples with a smaller bead diameter of 0.003” were used for hot and cold temperature measurements. The hot side thermocouple (TC2) was attached at the edge where the wide end and narrow support mid-section meet. As shown in Figure 17, a small amount of silver paint connected the tip of the thermocouple to the surface of the kapton. Super glue was applied to the insulated thermocouple wire to ensure that the kapton sample holder was durable enough to handle during the vacuum chamber mounting process.

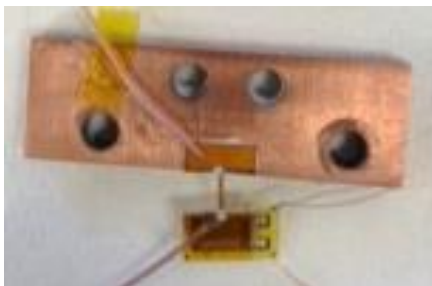


**Figure 17: Thermocouples attached to kapton sample holder with silver paint**

The baseline set-up and removable copper block were then attached to the cryostat stage, as seen in Figure 18. From there, power was supplied to the heater. The cryostat stage, commonly referred to as the cold finger, consists of 10 pins. These pins allow for electrical connections to be made. Using four of the cold finger pins, 0.003” diameter copper wire was soldered onto female pin covers. It was recommended by the Janis Research Company to solder the copper wires onto female pin covers rather than directly onto the cold finger pins. Two 0.003” diameter copper wires were soldered to each linear strain gage heater solder pad. One set of copper wires determined the current flowing through the heater while the other set determined the heater voltage.

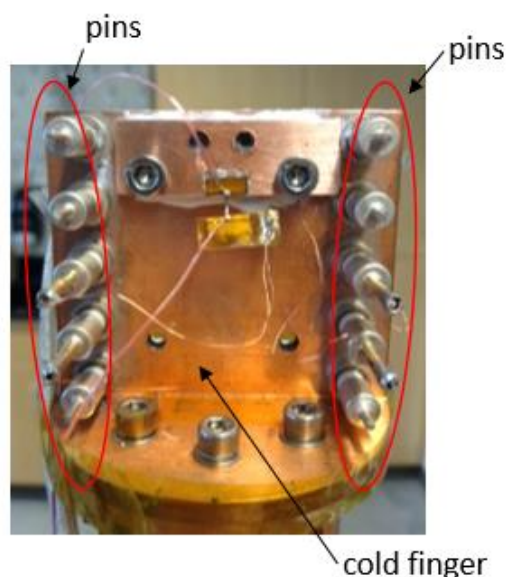


**Figure 18: Baseline parallel thermal conductance set-up**

Performing the parallel thermal conductance measurements in a cryostat vacuum chamber (Janis Research Co. CCS-400H/204) helped to avoid convection losses. An Edwards vacuum pump was used to achieve an environment of 5E-05 Torr. In addition, a radiation shield was attached to the vacuum chamber to avoid radiation losses. Using an Agilent E3631A power source and a custom Labview program, various step voltages between 0.3-1 V were applied to the linear strain gage heater while the hot and cold side temperatures were recorded. The power of the linear strain gage heater was determined, using equation 2-1.

$$P = I^2 R = C_{baseline} \Delta T \quad [2-1]$$

Fitting the linear relation between the heater power and temperature difference, the baseline thermal conductance could be determined, as shown in Figure 19. Measuring the baseline accounts for all background thermal conduction losses, including the conduction losses from the thermocouples and heater lead wires. The baseline was measured more than once for various steady-state durations in order to ensure reproducibility.

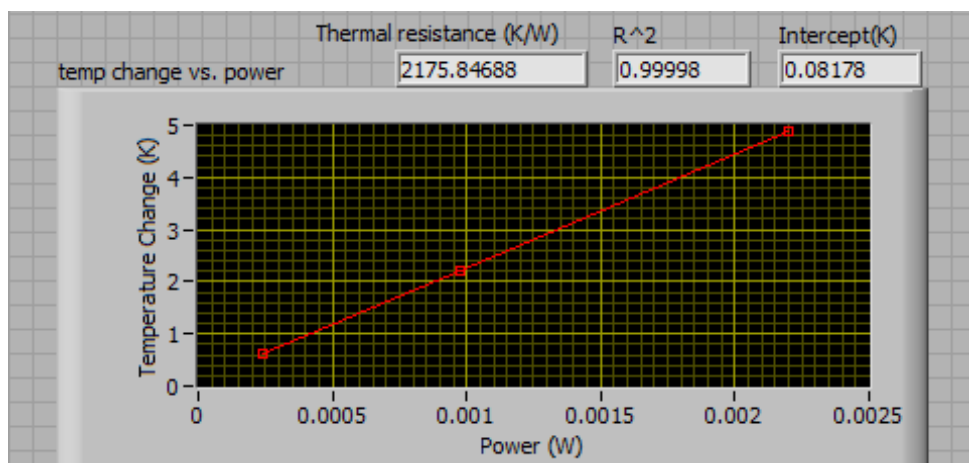


**Figure 19:** An example of the linear relation between power from the heater and the temperature change in the sample

Once the baseline for the parallel thermal conductance measurement was completed, the sample could then be attached.  $\text{Bi}_2\text{Te}_{2.8}\text{Se}_{0.2}$  paste pellets were first cut into rectangular shapes that were roughly 12 mm x 3 mm x 0.7 mm. These paste pellets were fabricated using an n-type ThermoAura powder that utilized a bottom-up assembly with a microwave-stimulated wet-chemical method. From there, the powder was synthesized into screen printable ink and cold-pressed into pellet form. Additional details of the screen printable ink are included in Section 3.4.1.

The sample was placed directly above the cold side copper block and hot side heater. Applying additional silver paint directly on top of the hot and cold side thermocouple helped achieve a good thermal contact. Slight pressure was applied to the brittle  $\text{Bi}_2\text{Te}_{2.8}\text{Se}_{0.2}$  pellet while the silver paint cured on a 60°C hotplate for 30 minutes.

After curing the silver paint, the set-up was re-mounted onto the cold finger using the removable copper block, as shown in Figure 20. The measurement method used to measure the baseline was repeated, this time to determine the total conductance,  $C_{\text{total}}$ . From there, the net thermal conductance could be calculated as  $C_{\text{net}} = C_{\text{total}} - C_{\text{baseline}}$ , resulting in the thermal conductance of just the  $\text{Bi}_2\text{Te}_{2.8}\text{Se}_{0.2}$  paste pellet. The thermal conductivity was then determined using equation 2-2.

$$K = (C_{\text{total}} - C_{\text{baseline}}) \cdot L/A \quad [2-2]$$

where  $L$  is the distance between the hot and cold side thermocouples and  $A$  is the cross-sectional area of the  $\text{Bi}_2\text{Te}_{2.8}\text{Se}_{0.2}$  paste pellet.

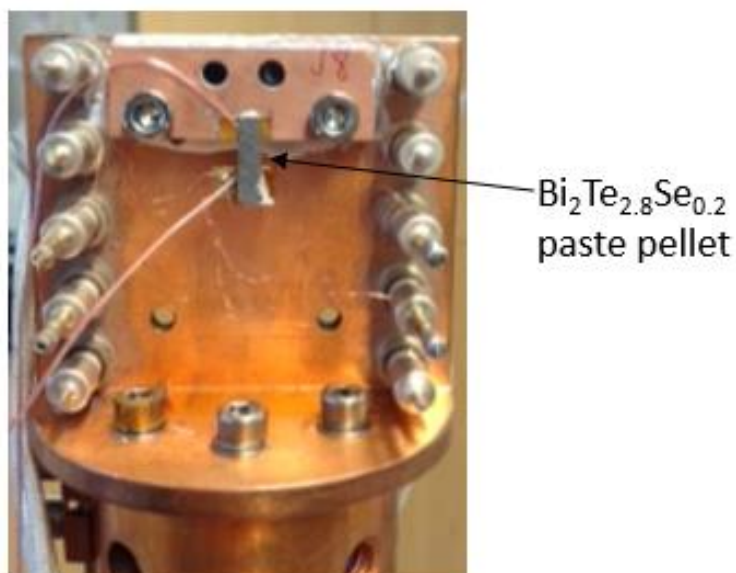


**Figure 20: Total parallel thermal conductance set-up**

## 2.2 Results and Discussion of Thermal Conductivity

### 2.2.1 Measurement of Calibration Samples

Prior to measuring the  $\text{Bi}_2\text{Te}_{2.8}\text{Se}_{0.2}$  paste pellet, samples with known thermal conductivities were measured in order to calibrate the measurement system. Table 1 shows the various reference samples measured using the parallel-thermal conductance method (PTC) compared to their reference value (reference). These calibration samples were measured multiple times in order to ensure the repeatability and accuracy of the results. In addition, both the baseline and total thermal conductance were measured between 5-10 times to ensure consistency and thermal equilibrium had been obtained.

**Table 1: Calibration thermal conductivity samples**

Material	$C_{\text{total}}$ (W/K)	$C_{\text{baseline}}$ (W/K)	A ( $\text{mm}^2$ )	L (mm)	$K_{\text{PTC}}$ (W/mK)	$K_{\text{reference}}$ (W/mK)
Alumina	5.97E-03	3.34E-03	2.61	24.85	24.98	24.7
Microscope glass slide	1.60E-03	4.22E-04	2.52	3.00	1.40	1.20

The parallel thermal conductance technique is a relatively easy and reproducible method for measuring the thermal conductivity of free-standing samples, such as  $\text{Bi}_2\text{Te}_{2.8}\text{Se}_{0.2}$  paste pellets. No additional sample treatment or preparation is necessary unlike many of the other thermal conductivity measurement methods which may require lithography or sputter deposition. Mounting the heater and thermocouples requires a delicate hand in order to deposit a minimal amount of silver paint yet ensure proper attachment to the kapton sample holder. In addition, the  $\text{Bi}_2\text{Te}_{2.8}\text{Se}_{0.2}$  paste pellet is extremely brittle and much care needs to be taken in order to attach the sample on top of the thermocouples while applying enough pressure to create sufficient thermal contact with the removable copper block and heater.

### 2.2.2 Measurement of $\text{Bi}_2\text{Te}_{2.8}\text{Se}_{0.2}$ Paste Pellet

Prior to measuring the thermal conductivity of the paste pellets using the parallel thermal conductance method, the pellets were measured using the LFA 1000 Laser Flash Apparatus (Thermal Conductivity / Diffusivity). This instrument required the fabrication of a 13 mm diameter  $\text{Bi}_2\text{Te}_{2.8}\text{Se}_{0.2}$  paste pellet with a thickness around 700  $\mu\text{m}$  in order to fit the sample holder. The cross-plane thermal diffusivity of the paste pellet was then measured using the commercial laser flash instrument. In order to calculate the cross-plane thermal conductivity, the density and specific heat of the pellet must be known. The sample density could be determined using the Archimedes method, while the specific heat was determined using a commercial differential scanning calorimeter instrument.

Once the cross-plane thermal conductivity was determined, the in-plane thermal conductivity could be measured using the above mentioned parallel thermal conductance method. For this in-plane thermal conductivity method, the paste pellet needed to be cut

into a narrow rectangular shape. Therefore, the circular paste pellet was cut into a 12 mm x 3 mm rectangle using a diamond wafer saw. Figure 21 and Figure 22 show the baseline and total thermal conductance for pellets A and B, respectively. Accuracy in the thermal conductivity measurement can be obtained by minimizing the baseline thermal conductance. As a result, the difference between the baseline and total thermal conductance is maximized in order to provide adequate measurement sensitivity.

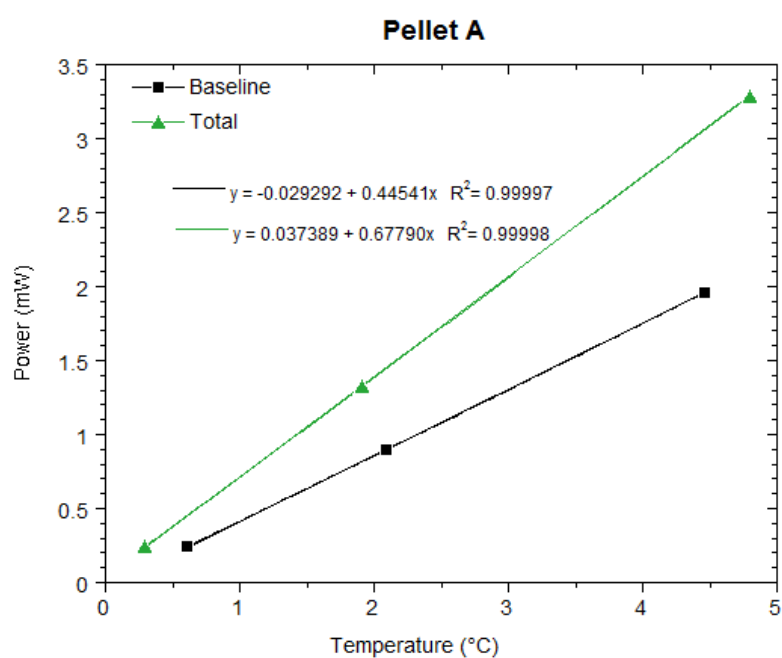


**Figure 21: Baseline and total thermal conductance of pellet A**

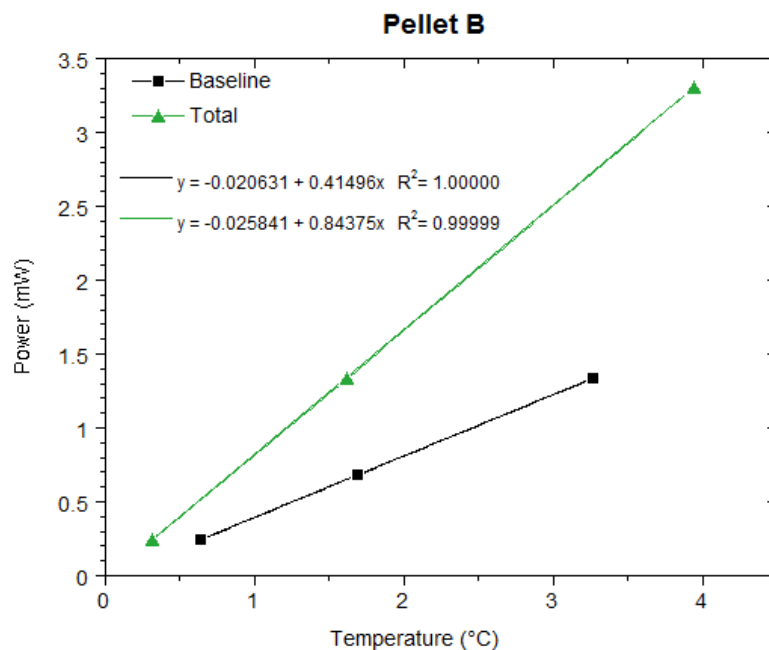


**Figure 22: Baseline and total thermal conductance of pellet B**

Table 2 compares the data for the two  $\text{Bi}_2\text{Te}_{2.8}\text{Se}_{0.2}$  paste pellets based on the parallel-thermal conductance method (PTC) and laser flash method (LFA). The baseline and total thermal conductance were measured approximately 5-10 times in order to ensure that thermal equilibrium and good consistency were achieved. The parallel thermal conductance method exhibits a maximum difference of 5.3% from the laser flash method, demonstrating good agreement between the two thermal conductivity measurement methods. This indicates that the  $\text{Bi}_2\text{Te}_{2.8}\text{Se}_{0.2}$  paste pellets are isotropic. In addition, the total uncertainty of the pellets was calculated to be less than  $2.31\text{E-}06$  W/mK.

**Table 2:  $\text{Bi}_2\text{Te}_{2.8}\text{Se}_{0.2}$  paste pellet thermal conductivity**

Material	$C_{\text{total}}$ (W/K)	$C_{\text{baseline}}$ (W/K)	A ( $\text{mm}^2$ )	L (mm)	$K_{\text{PTC}}$ (W/mK)	$K_{\text{LFA}}$ (W/mK)	% Difference
Pellet A	6.77E-04 $\pm 2.51\text{E-}05$	4.47E-04 $\pm 2.13\text{E-}05$	1.95 $\pm 1\text{E-}06$	3.50 $\pm 0.1$	0.39 $\pm 2.31\text{E-}06$	0.39	1.12
Pellet B	8.43E-04 $\pm 2.82\text{E-}05$	4.15E-04 $\pm 2.00\text{E-}05$	2.72 $\pm 1\text{E-}06$	3.20 $\pm 0.1$	0.50 $\pm 7.69\text{E-}07$	0.53	5.30

The different thermal conductivities between Pellet A and Pellet B are attributed to the different annealing conditions despite being fabricated from the same ink. Pellet A was annealed at 430°C for 15 minutes, while Pellet B was annealed at 430°C for 45 minutes. Both pellets were annealed in a vacuum environment. Pellet B exhibits a higher thermal conductivity than pellet A due to the longer annealing duration. With a longer annealing duration, additional sintering occurs that increases the connections between the nanoplates, resulting in less voids and pores throughout the film. As a result, the improved film connectivity leads to a higher thermal conductivity.

### 2.2.3 Measurement of $\text{Bi}_2\text{Te}_{2.8}\text{Se}_{0.2}$ Film

After successfully confirming and measuring  $\text{Bi}_2\text{Te}_{2.8}\text{Se}_{0.2}$  paste pellets using the parallel thermal conductance method,  $\text{Bi}_2\text{Te}_{2.8}\text{Se}_{0.2}$  thick films were measured.  $\text{Bi}_2\text{Te}_{2.8}\text{Se}_{0.2}$  thick flexible films were screen printed using the same paste composition for the pellet. As mentioned in the above section,  $\text{Bi}_2\text{Te}_{2.8}\text{Se}_{0.2}$  is an extremely brittle material. As a result, the thick films were screen printed onto a 50  $\mu\text{m}$  thick kapton substrate. The films exhibited a uniform thickness between 10-20  $\mu\text{m}$  thick, depending on the screen mesh size used.

The parallel thermal conductance method was used to determine the baseline measurement of the set-up. From there, the thick film sample was attached to the top of the kapton sample holder and thermocouples with silver paint (Figure 23). The total conductance was then measured. Using equation 1-8, the thermal conductivity of the  $\text{Bi}_2\text{Te}_{2.8}\text{Se}_{0.2}$  thick film sample was determined to be 10.34 W/mK. However, since the same paste composition was used for both the pellet and film, the in-plane thermal conductivity is expected to be the same for both types of samples.



**Figure 23: Parallel thermal conductance set-up with  $\text{Bi}_2\text{Te}_{2.8}\text{Se}_{0.2}$  film**

When analyzing the reason for a higher thermal conductivity for the film compared to the paste pellet, it can be seen that the main difference is the included kapton substrate for the thick film. Since kapton is a thermal insulator with a thermal conductivity of 0.12 W/mK, the heat flowing through this set-up must first travel through the 50  $\mu\text{m}$  thick kapton. Mounting the sample with the kapton and heater in direct contact prevents a direct path for the heat to travel from the heater to the  $\text{Bi}_2\text{Te}_{2.8}\text{Se}_{0.2}$  film.

In order to improve the thermal contact between the heater and film, the sample was rotated 180°. This allowed the heater and  $\text{Bi}_2\text{Te}_{2.8}\text{Se}_{0.2}$  film to be directly in contact (Figure 24). Measuring the total conductance of the improved set-up, the thermal conductivity of the  $\text{Bi}_2\text{Te}_{2.8}\text{Se}_{0.2}$  film was calculated to be 0.97 W/mK. This data demonstrates that the insulating kapton dramatically influenced the thermal conductivity

measurement despite a thickness of 50  $\mu\text{m}$ . Although this is an improvement in measuring the thermal conductivity, the in-plane thermal conductivity for the film is still higher than the expected value. This also indicates that there are still excess heat conduction losses that prevent the parallel thermal conductance method from being sensitive enough to measure films with a thickness of 10-20  $\mu\text{m}$ . The thermal conductance of the thermocouple wires is calculated to be approximately  $3.48\text{E-}05$  W/K. However, the thermal conductance of the thick films is estimated to be  $4.95\text{E-}06$  W/K. Therefore, the higher thermal conductance from the thermocouples proves that the heat loss through the thermocouples is much greater than the heat flow through the thick film sample.



**Figure 24:** Revised parallel thermal conductance set-up with  $\text{Bi}_2\text{Te}_{2.8}\text{Se}_{0.2}$  film

## CHAPTER 3: SEEBECK COEFFICIENT AND ELECTRICAL CONDUCTIVITY

### MEASUREMENT OF THIN AND THICK FILMS

#### 3.1 Experimental Methods of Seebeck Coefficient and Electrical Conductivity

A commercial LSR-3 Linseis – Seebeck Coefficient & Electric Resistivity (LSR) instrument was used to measure the power factor of various thin film thermoelectric materials, as shown in Figure 25. The primary function of the LSR is to simultaneously measure the Seebeck coefficient and electrical resistivity of bulk thermoelectric samples within a temperature range from room temperature up to 1500°C. Using a measurement adapter, the power factor of flexible films can also be determined.



**Figure 25:** LSR-3 Linseis - Seebeck coefficient & electric resistivity [image courtesy of Linseis website]

In order to measure the power factor, the sample is vertically clamped between two electrodes. Figure 26 shows that the upper electrode is the cold side while the lower electrode contains a heater in order to form the hot side. Thus, a temperature gradient is created between the two electrodes. Two spring loaded thermocouples make contact with

the film surface to measure the temperature gradient and induced thermoelectric voltage in order to determine the Seebeck coefficient. When measuring the electrical resistivity, a constant current is applied to the electrodes while the thermocouples measure the change in voltage. The entire measurement set-up is located in a furnace, allowing for the properties to be determined at various temperature profiles in an inert gas environment.

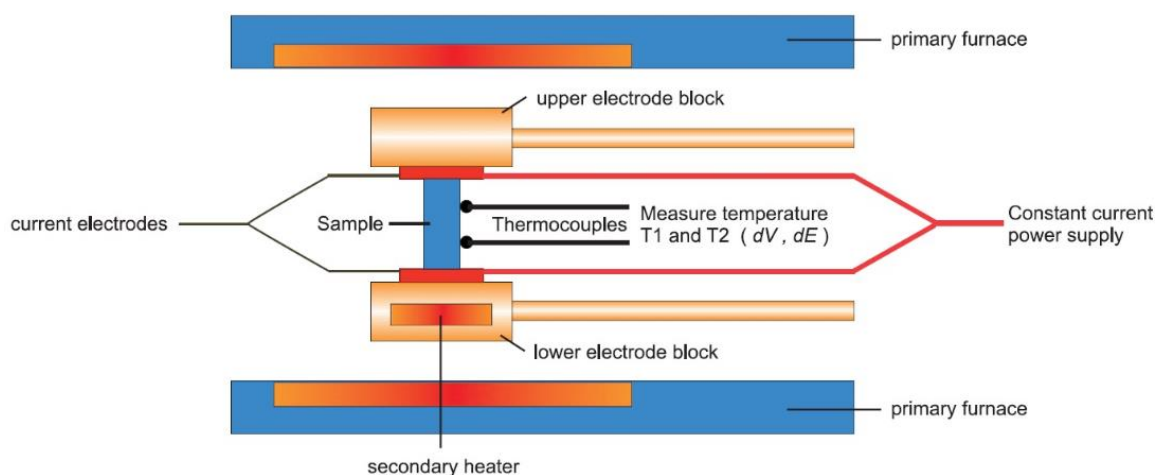


**Figure 26: LSR measurement set-up [image courtesy of Linseis website]**

When measuring the Seebeck coefficient and electrical resistivity of flexible films, an adapter had to be used to ensure good electrical contact with the electrodes. Typically, the thin films were deposited onto a rigid substrate, such as alumina. By depositing the thermoelectric materials onto a rigid substrate, the sample mounting process became less time consuming. In addition, since the ink composition remained the same for films deposited on a rigid or flexible substrate, the thermoelectric properties would also be the same.

Before depositing thin films onto a rigid substrate, the experimental temperature range had to first be considered. If the temperature range was too high, the substrate could soften or melt, thus damaging the instrument. In addition, the film could not be

deposited on a substrate that was electrically conductive or had a Seebeck coefficient. Otherwise, the measured properties would be influenced by the rigid substrate. Figure 27 shows a sample mounted in stainless steel film adapter clamps purchased from Linseis. These adapter clamps allowed the electrode to pass current to the surface of the thin film sample, while creating an in-plane temperature gradient throughout the sample.



**Figure 27: LSR thin film adapters**

### **3.2 Study of $\text{Bi}_2\text{Te}_3$ and $\text{Cu}_2\text{Se}$ Spin Coated Thin Films**

#### 3.2.1 Material Synthesis

A collaboration with the University of California, Los Angeles (UCLA) was developed during this study.  $\text{Bi}_2\text{Te}_3$ ,  $\text{Cu}_2\text{Se}$ , and  $\text{Cu}_2\text{S}$  thin films were synthesized using either a wet chemistry approach to develop two-dimensional nanoplate powder or commercial powders [54, 55]. These powders were dispersed in a solution to create colloidal inks used for spin coating. The thickness of the thin films ranged from 60 nm up to 240 nm, depending on the number of spin coating layers. Samples were annealed at various temperatures between 300-500°C in order to determine the maximum peak power factor. The power factor of these samples were then measured using the LSR. Due to such small thicknesses, many problems achieving good electrical and thermal contact had to be overcome.

### 3.2.2 Experimental Results and Discussion on Spin Coated Thin Films

#### 3.2.2.1 $\text{Bi}_2\text{Te}_3$

Figure 28 and Figure 29 show multiple temperature profile measurements for  $\text{Bi}_2\text{Te}_3$  annealed at  $350^\circ\text{C}$  on an alumina ( $\text{Al}_2\text{O}_3$ ) substrate from room temperature up to  $250^\circ\text{C}$ . The representative Seebeck coefficient and electrical conductivity curves do not show any repeatability between each test. In particular, it is expected that the Seebeck coefficient curve for thin films should exhibit a smoother curve similar to the Test 4 Seebeck coefficient curve. To improve the repeatability, samples were either completely remounted in the clamps, only the thermocouple contacts were adjusted, or the sample was not touched at all. However, all three different sample mounting approaches continued to result in poor repeatability.

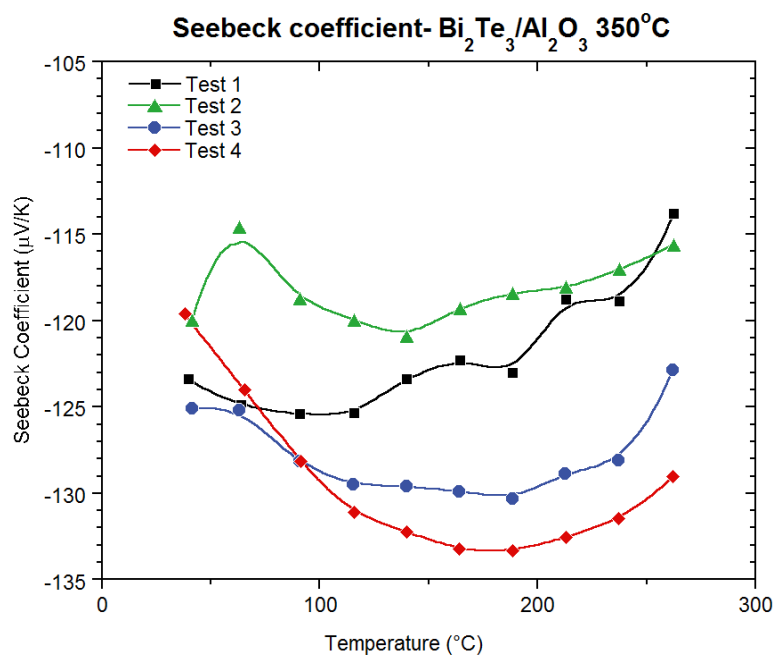


**Figure 28:** Seebeck coefficient  $\text{Bi}_2\text{Te}_3/\text{Al}_2\text{O}_3$   $350^\circ\text{C}$

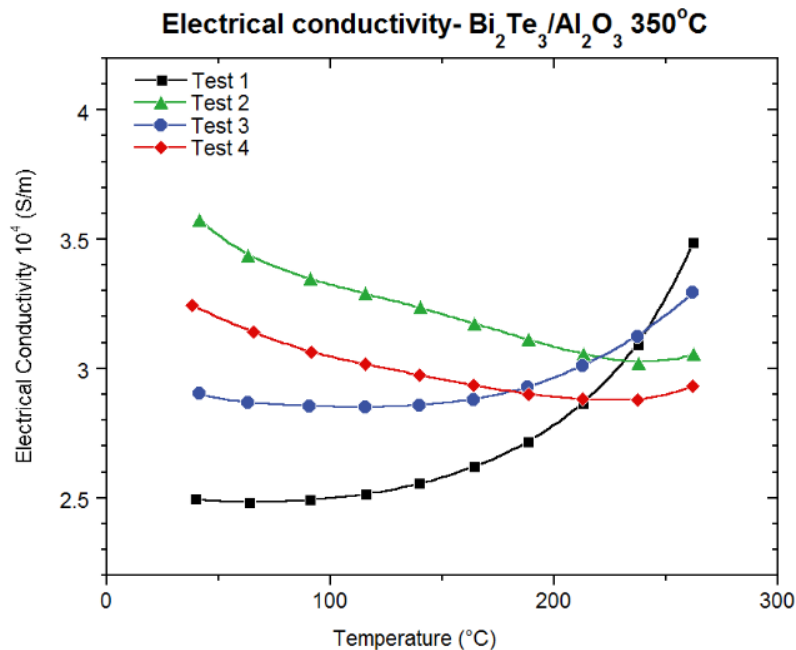


**Figure 29: Electrical conductivity  $\text{Bi}_2\text{Te}_3/\text{Al}_2\text{O}_3$  350°C**

It was observed that after one temperature profile measurement, the thermocouples would typically lose contact with the sample. Upon closer inspection, it can be seen that the thermocouples would remove a portion of the sample, resulting in visible scratches (Figure 30). This is due to the sample being only a couple hundred nanometers thin and the amount of pressure applied to the thermocouples. By removing portions of the sample, both the electrical conductivity and Seebeck measurements became unrepeatable.

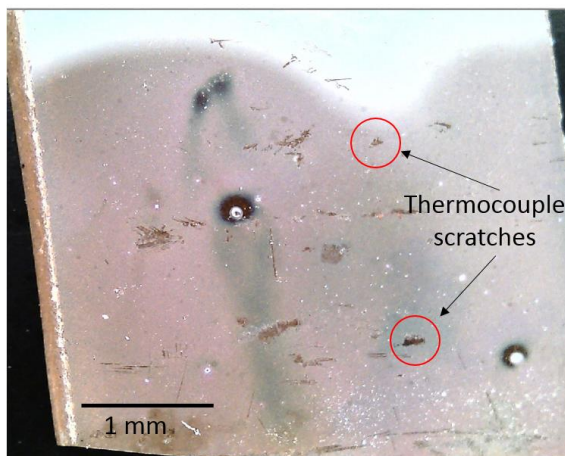


**Figure 30: Thermocouple damage**

As an attempt to primarily focus on achieving a smoother Seebeck curve, various changes were made to the thermocouples, which included graphite covers and graphite stencils. Graphite was selected to cover the thermocouples since it would help improve the thermal contact yet maintain a strong electrical contact.

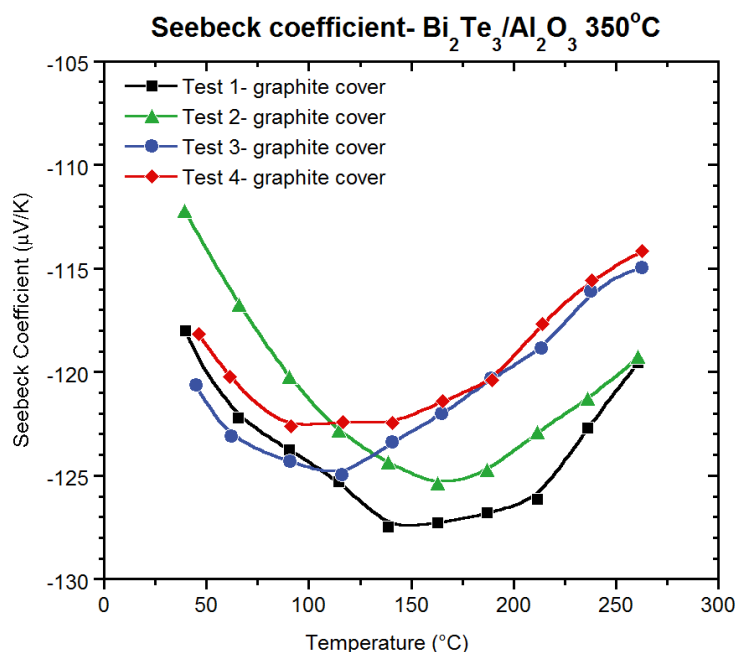
Graphite covers were fabricated using 0.25 mm thick graphite foil. Creating a graphite cover would prevent the thermocouples from penetrating through the thin sample surface. The cover was designed to be long enough in order to stay on the thermocouple without any assistance (Figure 31). After gently placing the cover onto the tip of the thermocouple, the thermocouples/graphite covers were slowly brought into contact with the surface of the sample.



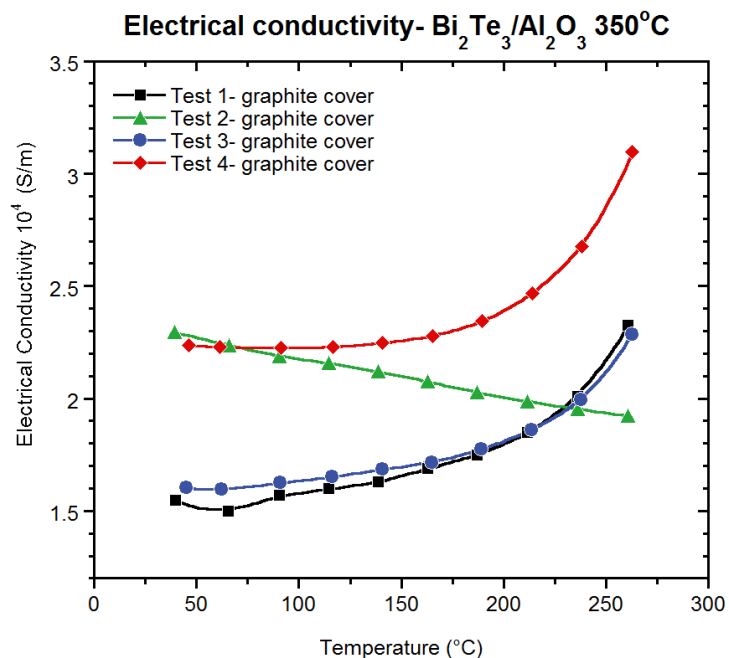
**Figure 31: Schematic of graphite cover**

Figure 32 and Figure 33 show the Seebeck coefficient and electrical conductivity curves when using graphite covers. The Seebeck coefficient graph exhibits a smoother

curve, indicating that the graphite covers slightly improved the thermal contact. However, the lack of repeatability for the Seebeck coefficient and electrical conductivity curves indicate that the electrical contact is still not ideal. In addition, it was noticed that after removing the thermocouples from the sample, the graphite covers adhered to the sample surface (Figure 34). This adherence may be due to the amount of pressure and the elevated temperature that occurs during the measurement process. As a result, removal of the graphite covers also removes the thin film, causing additional damage to the sample.



**Figure 32:** Seebeck coefficient  $\text{Bi}_2\text{Te}_3/\text{Al}_2\text{O}_3$  350°C graphite covers



**Figure 33: Electrical conductivity  $\text{Bi}_2\text{Te}_3/\text{Al}_2\text{O}_3$  350°C graphite covers**



**Figure 34: Graphite cover adhering to sample surface**

Further examination of the graphite covers led to the realization that the contact distance between the two thermocouples was no longer accurate. Since the graphite covers have such a large contact area, it was extremely difficult to identify the exact location the thermocouples were touching the surface sample. In addition, formation of the graphite covers from graphite foil created multiple “points” at the end of the cover. As a result, each time the graphite covers were brought into contact with the sample

surface, the contact distance changed. Figure 35 shows an exaggerated schematic of the graphite cover and sample contact.

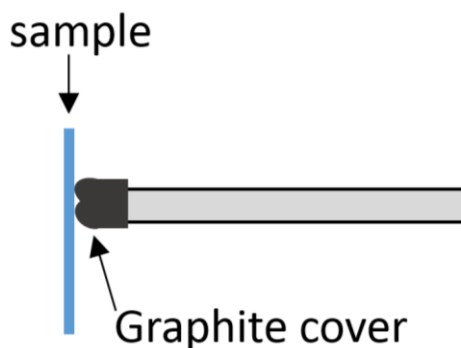


**Figure 35:** Schematic of exaggerated graphite cover and sample contact

In order to further improve the electrical contact without interfering with the ability to accurately determine the exact thermocouple contact length, a graphite stencil design was developed. The graphite stencil was placed over the top of a sample, acting as a shadow mask. Liquid graphite was then sprayed onto the surface of the sample, creating the pattern shown in Figure 36. Prior to selecting liquid graphite, gold was sputtered onto the sample surface using the same stencil pattern. However, depositing gold onto the surface of a thermoelectric sample resulted in a non-Ohmic contact.

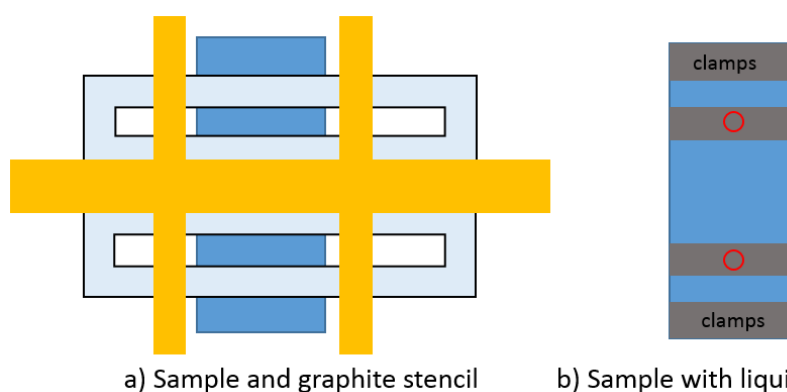


**Figure 36:** a) before and b) after liquid graphite deposition (red circles indicate thermocouple placement)

The electrode clamp region was also sprayed with liquid graphite in order to improve electrical contact between the electrode clamps and sample. The thermocouple contact region are the two inner strips of liquid graphite, indicated by the red circles in Figure 36. It is extremely easy to remove the liquid graphite from the sample surface, so it was desired to only bring the thermocouples into contact with the surface as few times as possible.

In order to determine the Seebeck coefficient and electrical conductivity, corrections needed to be made to the LSR measurement results. Since graphite has a high electrical conductivity, the true electrical distance should be at the inner edges of the graphite rather than the thermocouple contact distance, as shown in Figure 37.

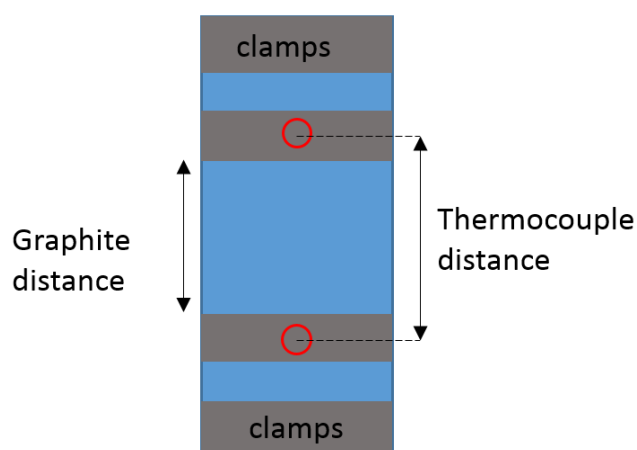


**Figure 37: Corrected distance**

Using equations 3-1 and 3-2, the corrected Seebeck and electrical conductivity could be calculated, respectively.

$$S_{\Delta D} = S \frac{\Delta L}{\Delta D} \quad [3-1]$$

$$\sigma_{\Delta D} = \sigma \frac{\Delta D}{\Delta L} \quad [3-2]$$

where  $S$  is the uncorrected Seebeck coefficient,  $\sigma$  is the uncorrected electrical conductivity,  $\Delta L$  is the thermocouple length, and  $\Delta D$  is the graphite length.

### 3.2.2.2 $\text{Cu}_2\text{Se}$

Throughout the collaboration, interest shifted towards measuring the thermoelectric properties of  $\text{Cu}_2\text{Se}$  films sent from our collaborators. Therefore, the graphite stencil method was applied to  $\text{Cu}_2\text{Se}$  samples. The Seebeck coefficient and electrical conductivity of a  $\text{Cu}_2\text{Se}$  sample are shown in Figure 38 and Figure 39. Both curves are much smoother, indicating an increased repeatability compared to the graphite cover results. However, the repeatability between tests 2-5 still do not reflect an accuracy within 10%. Therefore, these results are not yet publication worthy.

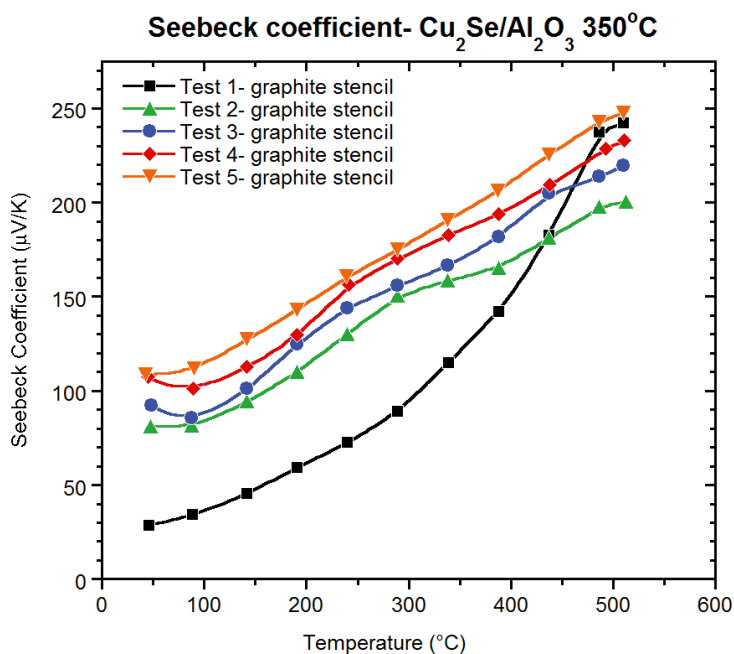


**Figure 38: Seebeck coefficient  $\text{Cu}_2\text{Se}/\text{Al}_2\text{O}_3$  graphite stencil**

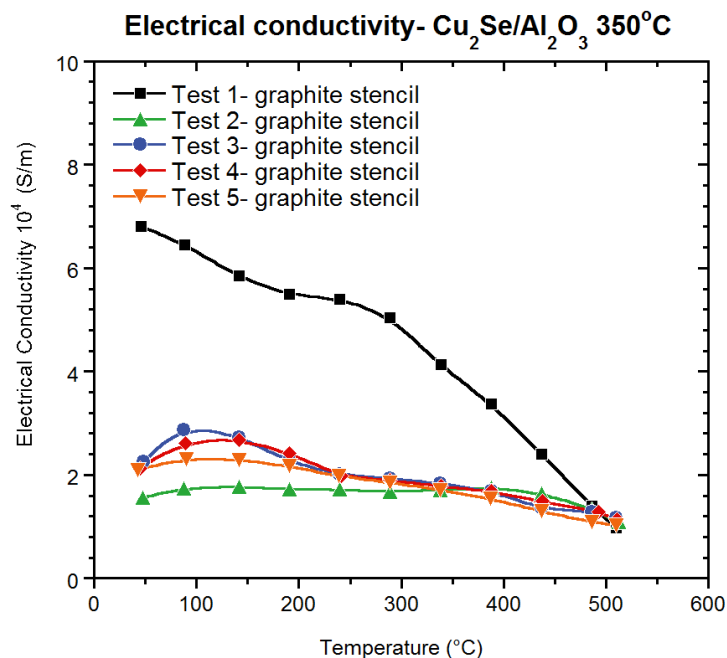


**Figure 39: Electrical conductivity  $\text{Cu}_2\text{Se}/\text{Al}_2\text{O}_3$  graphite stencil**

These results provided UCLA with enough information to begin focusing on optimizing the material synthesis and annealing process for future  $\text{Cu}_2\text{Se}$  samples. In addition, the LSR was installed with new thermocouples and it was decided that contact with the sample should be minimized to prevent excess scratching of the surface. Therefore, once the thermocouples were in contact with the sample surface, no re-mounting was necessary unless electrical contact was lost. Previously, the sample was re-mounted in the clamps and then the thermocouples were re-applied to the surface to prove repeatability between experiments. However, the increasingly scratched surface led to many more contact issues.

When using the new thermocouples, the thermocouple pressure was decreased as well. Typically, all thermoelectric samples were measured using a given temperature profile at least three times. As seen in Figure 40 and Figure 41 **Error! Reference source not found.**, a representative  $\text{Cu}_2\text{Se}$  temperature profile for the Seebeck coefficient and

electrical conductivity show that test 1 always differs from test 2 and test 3. The detailed reason for the difference in test 1 is not yet clear. However, it is suspected to be related to the intrinsic instability of  $\text{Cu}_2\text{Se}$  when an electrical field is applied at an elevated temperature. After test 1, the samples are annealed for a second time, causing the thermoelectric properties to stabilize, which result in good agreement between test 2 and test 3. These results indicate that better electrical and thermal contacts are made with the samples. This may be attributed to the minimization of scratching the sample surface by re-mounting as little as possible and decreasing the thermocouple pressure, thus creating a more continuous surface, which is ideal for measurements.

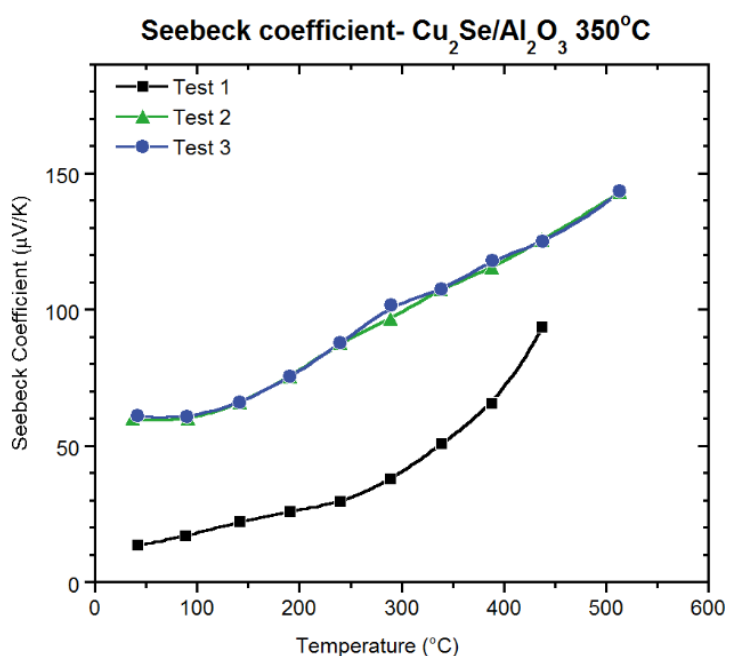


**Figure 40: Seebeck coefficient showing repeatability**

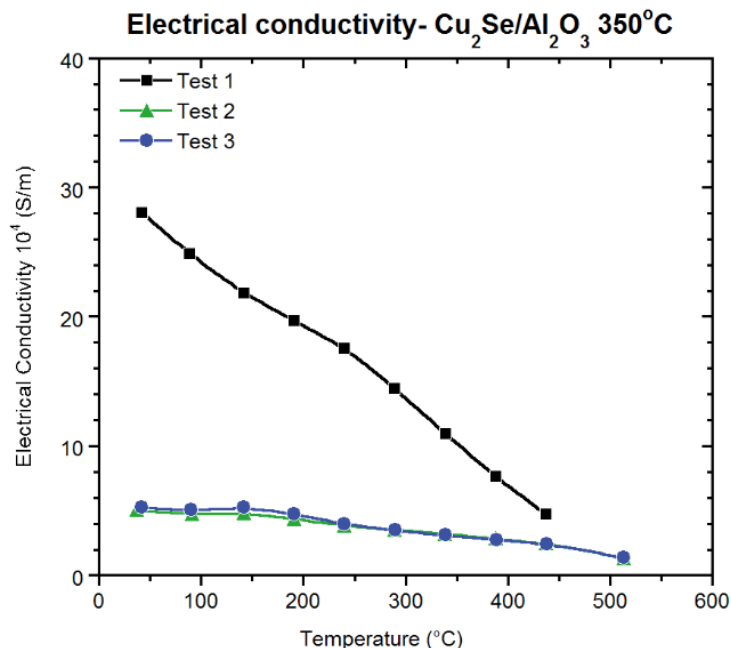
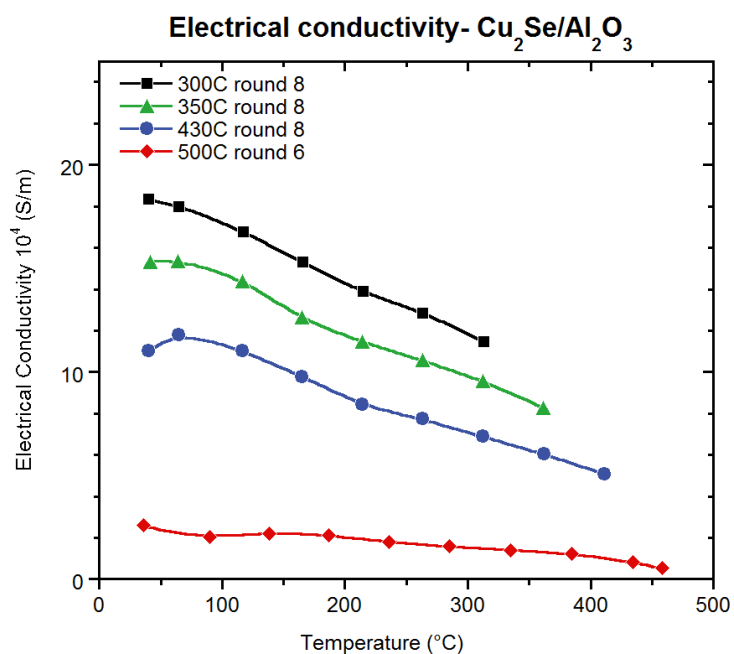


**Figure 41: Electrical conductivity showing repeatability**

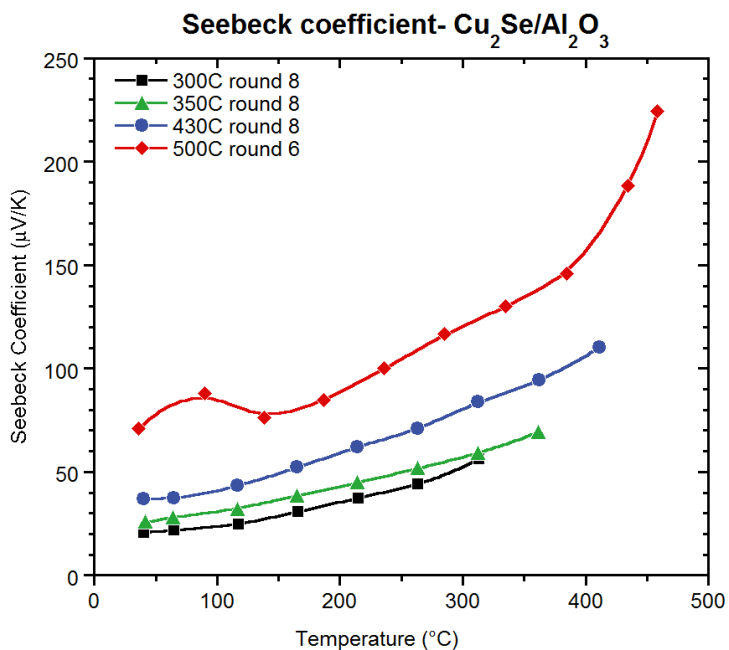
Once the changes in thermocouple contact with the surface were implemented, all samples were measured using this method. Several more samples were sent from UCLA in order to test the thermoelectric properties at various temperature ranges and confirm repeatability.

Figure 42, Figure 43, and Figure 44 show the best thermoelectric properties for samples annealed on a hotplate at  $300^\circ\text{C}$ ,  $350^\circ\text{C}$ ,  $430^\circ\text{C}$ , and  $500^\circ\text{C}$ . The entire material fabrication process was performed in a nitrogen-filled glovebox. Figure 42 shows that as the annealing temperature increases, the electrical conductivity decreases. This trend is attributed to a decrease in the charge carrier mobility. However, Figure 43 demonstrates that as the annealing temperature increases, so does the Seebeck coefficient. In addition, this graph also demonstrates that the new thermocouples and minimization of excess thermocouple contact with the sample created smoother Seebeck curves. As can be seen in Figure 44 **Error! Reference source not found. Error! Reference source not**

**found.Error! Reference source not found.**, the highest power factor is  $0.62 \text{ mW/mK}^2$  at  $411^\circ\text{C}$  when  $\text{Cu}_2\text{Se}$  is annealed at  $430^\circ\text{C}$ . The ultimate peak for the power factor curve was not determined since measuring past a temperature of  $430^\circ\text{C}$  would lead to additional sintering of the sample, which would alter the thermoelectric properties. Therefore, samples were measured to a maximum temperature of  $50^\circ\text{C}$  lower than the annealing temperature.



**Figure 42: Electrical conductivity of  $\text{Cu}_2\text{Se}/\text{Al}_2\text{O}_3$  at various annealing temperatures**



**Figure 43:** Seebeck coefficient of  $\text{Cu}_2\text{Se}/\text{Al}_2\text{O}_3$  at various annealing temperatures

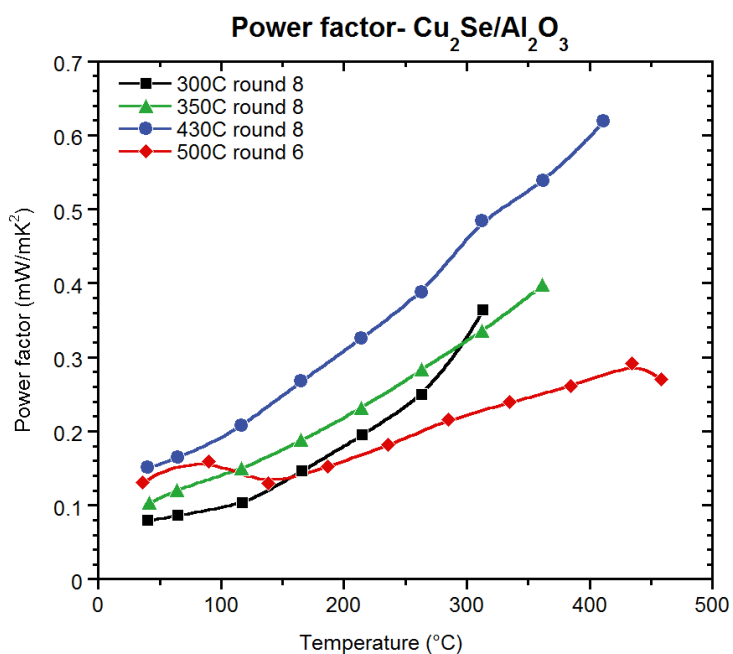


**Figure 44:** Power factor of  $\text{Cu}_2\text{Se}/\text{Al}_2\text{O}_3$  at various annealing temperatures

These final results will be submitted as part of a publication with UCLA. This publication will focus on the high thermoelectric properties of  $\text{Cu}_2\text{Se}$  flexible thin films annealed at  $430^\circ\text{C}$  in comparison to the other annealing temperatures.

### **3.4 Study of Bi<sub>2</sub>Te<sub>2.8</sub>Se<sub>0.2</sub> Screen Printed Thick Films**

#### **3.4.1 Material Synthesis**

Fabrication of n-type ThermoAura powder utilizes a bottom-up assembly with a microwave-stimulated wet-chemical method. Using a wet-chemical method creates bismuth telluride based nanoplates that have previously exhibited a high room temperature ZT of 1.1 by cold compaction and sintering of bulk pellets [56]. Due to the high bulk thermoelectric properties, this powder was synthesized into a screen printing paste to create thick flexible films.

The paste synthesis consisted of mixing the Bi<sub>2</sub>Te<sub>2.8</sub>Se<sub>0.2</sub> powder, a solvent (alpha terpineol), and binder (DisperBYK110) to create the ideal viscous and thixotropic inks for screen printing. To improve film adhesion to the substrate, glass powder was added to the ink. Finally, the ink was mixed using a planetary centrifugal mixer and vortex mixer to ensure uniform dispersion.

The films were printed onto flexible polyimide substrates, dried on a hotplate, and then cold compacted to increase the density of the film. From there, the films were sintered with no additional pressure. Experimenting with different annealing temperatures and time durations helped determine the annealing procedure for optimized thermoelectric properties.

#### **3.4.2 Experimental Results and Discussion of Screen Printed Thick Films**

##### **3.4.2.1 Various Annealing Temperatures**

To determine the ideal annealing temperature, temperatures between 420°C-450°C were studied. A maximum temperature of 450°C was chosen based on the melting temperature of the polyimide substrate. Thick film Bi<sub>2</sub>Te<sub>2.8</sub>Se<sub>0.2</sub> samples were screen

printed onto an alumina substrate in order to simplify the Seebeck coefficient and electrical conductivity measurements using the LSR. Each annealing temperature was held constant for 15 minutes in order to accurately compare the thermoelectric properties. The screen printed films, which had a uniform thickness between 10-20  $\mu\text{m}$ , were much thicker than the previously discussed spin coated samples. As a result, the thermoelectric properties were more consistent since increased pressure could be applied to the thermocouples without scratching the surface.

Figure 45 shows that the lowest annealing temperature of 420°C resulted in the highest Seebeck coefficient. All annealing temperatures above 420°C began to experience a decrease in the Seebeck coefficient property. However, annealing at a temperature of 430°C resulted in the highest electrical conductivity (Figure 46). A sudden improvement in the electrical conductivity of samples annealed at 420°C and 430°C suggests that at 430°C sintering occurs which increases the connections between the nanoplates to enhance the electrical conductivity property. However, annealing at 440°C or 450°C decreases the electrical conductivity. This may be due to tellurium evaporation that occurs with higher temperatures. As a result, the carrier concentration begins to decrease which also decreases the electrical conductivity. However, further measurements must be carried out in order to confirm this hypothesis.

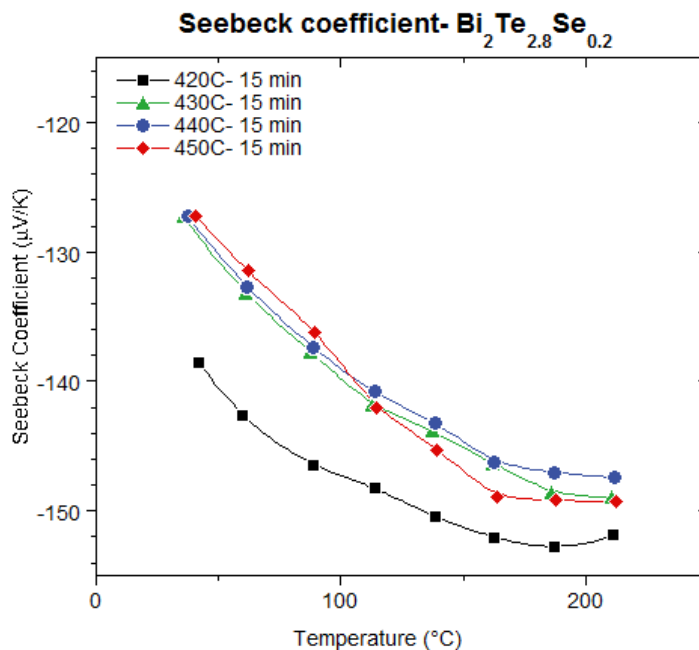


**Figure 45:** Seebeck coefficient of  $\text{Bi}_2\text{Te}_{2.8}\text{Se}_{0.2}$  at various annealing temperatures

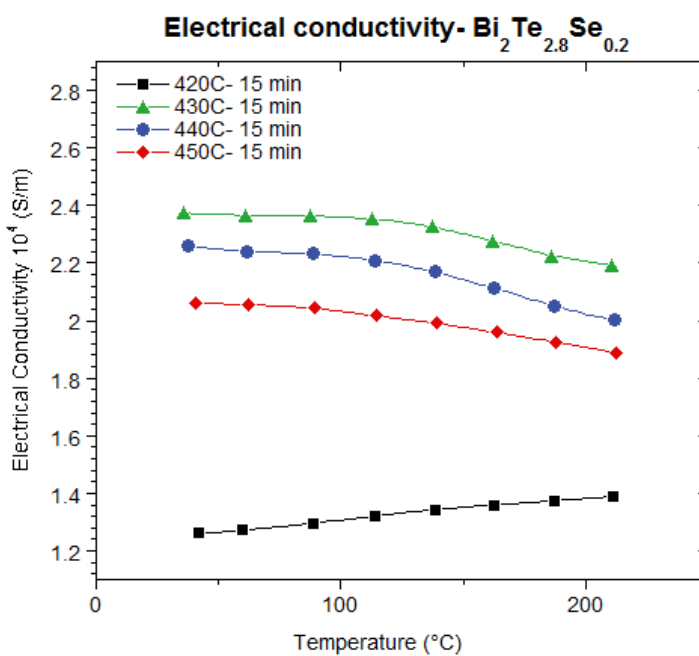


**Figure 46:** Electrical conductivity of  $\text{Bi}_2\text{Te}_{2.8}\text{Se}_{0.2}$  at various annealing temperatures

Calculating the power factor provides a better comparison between annealing temperatures. By comparing the power factor for each annealing temperature, Figure 47

confirms that the optimal annealing temperature is 430°C with a peak power factor of 0.49 mW/mK<sup>2</sup> at 186°C.

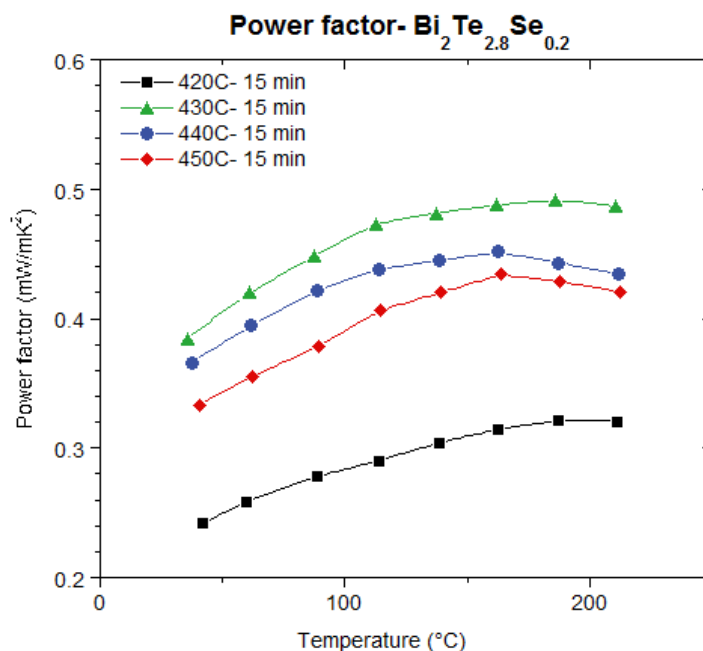


**Figure 47: Power factor of Bi<sub>2</sub>Te<sub>2.8</sub>Se<sub>0.2</sub> at various annealing temperatures**

#### 3.4.2.2 Various Annealing Durations at 430°C

Having selected 430°C as the ideal annealing temperature, the annealing duration must now be determined. Thick film samples were annealed for 15, 30, 45, 60, and 90 minutes. Initially, the Seebeck coefficient and electrical conductivity of all samples were measured using a custom-built testing system. Once it was determined which samples should be further tested, a temperature profile was run from room temperature up to 250°C using the LSR. In this case, only the 15, 45, and 60 minute annealing durations were measured using the LSR.

The highest Seebeck coefficient is approximately the same for both annealing durations of 15 and 45 minutes (Figure 48). However, the highest electrical conductivity is achieved with the 45 minute annealing duration (Figure 49). Holding the annealing

temperature at 430°C for 45 minutes allows the surfactant to be removed and the  $\text{Bi}_2\text{Te}_{2.8}\text{Se}_{0.2}$  film to sinter and densify. Therefore, with a 45 minute annealing duration, the peak power factor is  $0.56 \text{ mW/mK}^2$  at  $186^\circ\text{C}$  (Figure 50 Error! Reference source not found.).

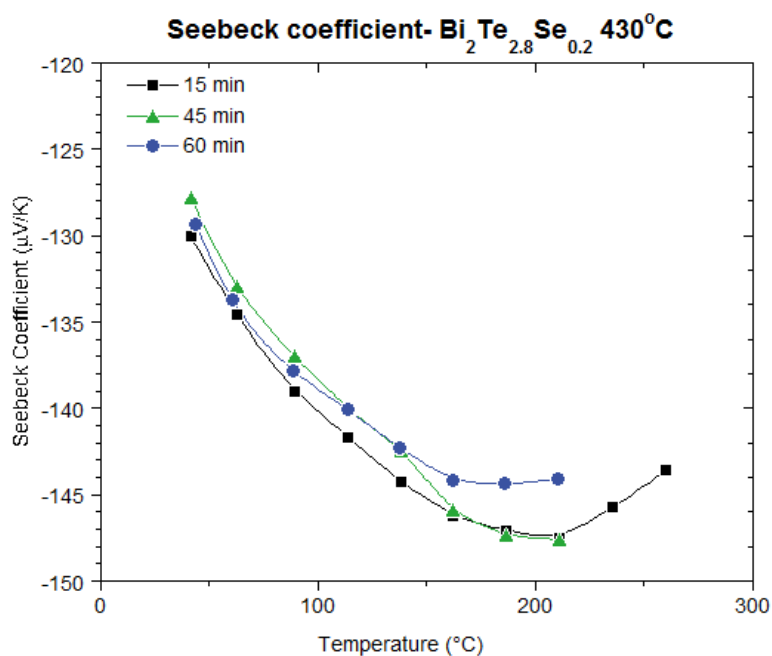


**Figure 48:** Seebeck coefficient of  $\text{Bi}_2\text{Te}_{2.8}\text{Se}_{0.2}$  annealed at  $430^\circ\text{C}$  for various annealing durations

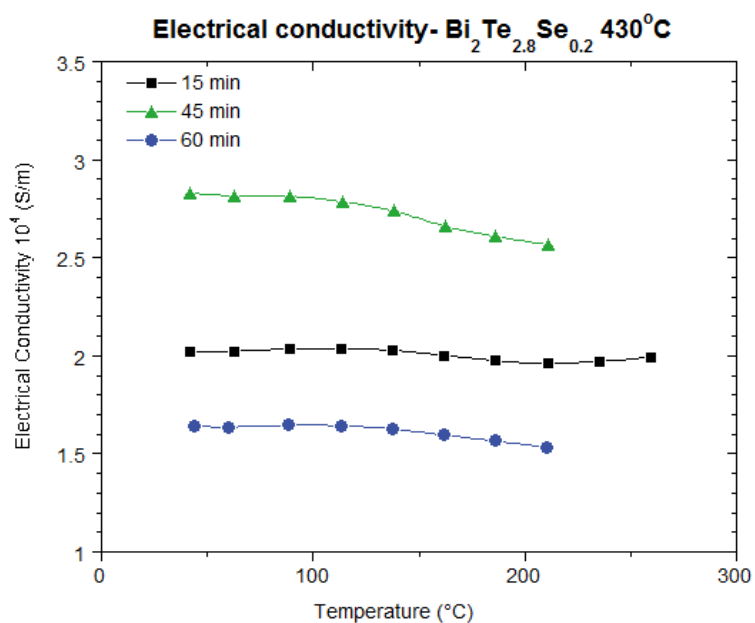


**Figure 49:** Electrical conductivity of  $\text{Bi}_2\text{Te}_{2.8}\text{Se}_{0.2}$  annealed at  $430^\circ\text{C}$  for various annealing durations

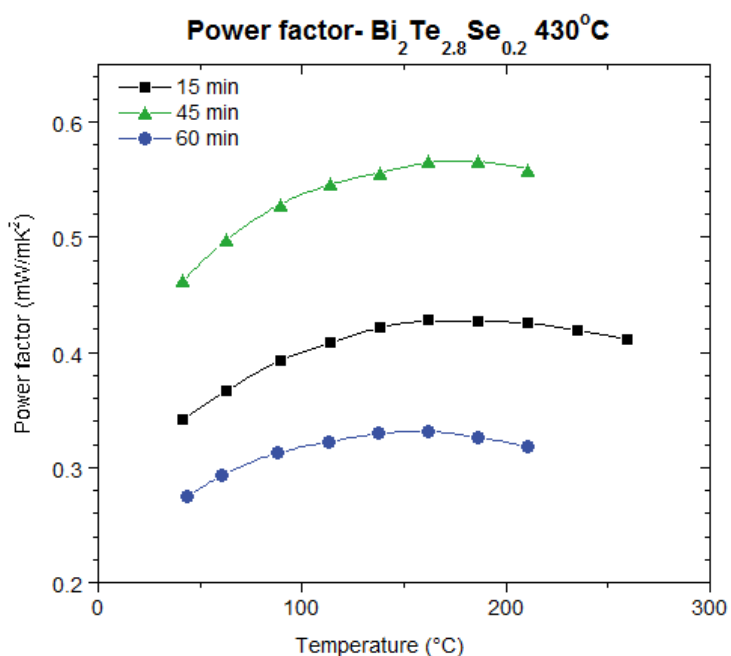


**Figure 50:** Power factor of  $\text{Bi}_2\text{Te}_{2.8}\text{Se}_{0.2}$  annealed at  $430^\circ\text{C}$  for various annealing durations

### 3.4.2.3 Figure of Merit of Screen Printed Thick Films

As previously discussed, the parallel thermal conductance method and commercial laser flash instrument demonstrated that the  $\text{Bi}_2\text{Te}_{2.8}\text{Se}_{0.2}$  paste pellet was isotropic. Therefore, the temperature-dependent cross-plane thermal conductivity was measured for the  $\text{Bi}_2\text{Te}_{2.8}\text{Se}_{0.2}$  paste pellet using the commercial laser flash instrument. Since both the paste pellet and thick films were fabricated using the same paste composition and annealing conditions, it was assumed that the thermal conductivity would be the same, regardless of the sample thickness. From there, the figure of merit for  $\text{Bi}_2\text{Te}_{2.8}\text{Se}_{0.2}$  could be determined from room temperature up to  $250^\circ\text{C}$ .

In order to compare the thick film thermoelectric properties, a  $500\ \mu\text{m}$  thick control pellet was made using pure nanocrystal powders. This control pellet was cold

pressed and sintered at 430°C for 45 minutes, in order to ensure similar annealing conditions to the thick film that exhibited the highest thermoelectric properties. As shown in Figure 51 graph (a), the electrical conductivity of the film is approximately 56% lower than the control pellet. This is due to the added glass powder and higher porosity in the thick film. As a result, the electron mobility decreases. Graph (b) shows that the Seebeck coefficient for both the control pellet and thick films are within 10% for the entire temperature profile, indicating that the carrier concentration is approximately the same. Due to the nanoscale grains and higher porosity, the thick film exhibits a lower thermal conductivity than the control pellet, as seen in graph (c). In addition, the added glass powder in the thick films cause phonon defects to scatter. Graph (d) shows the peak film ZT to be 0.43 at 175°C. Surprisingly, the control pellet only has a 20% higher ZT. This demonstrates that the drastically reduced thermal conductivity of the thick film compensates for the much lower electrical conductivity.

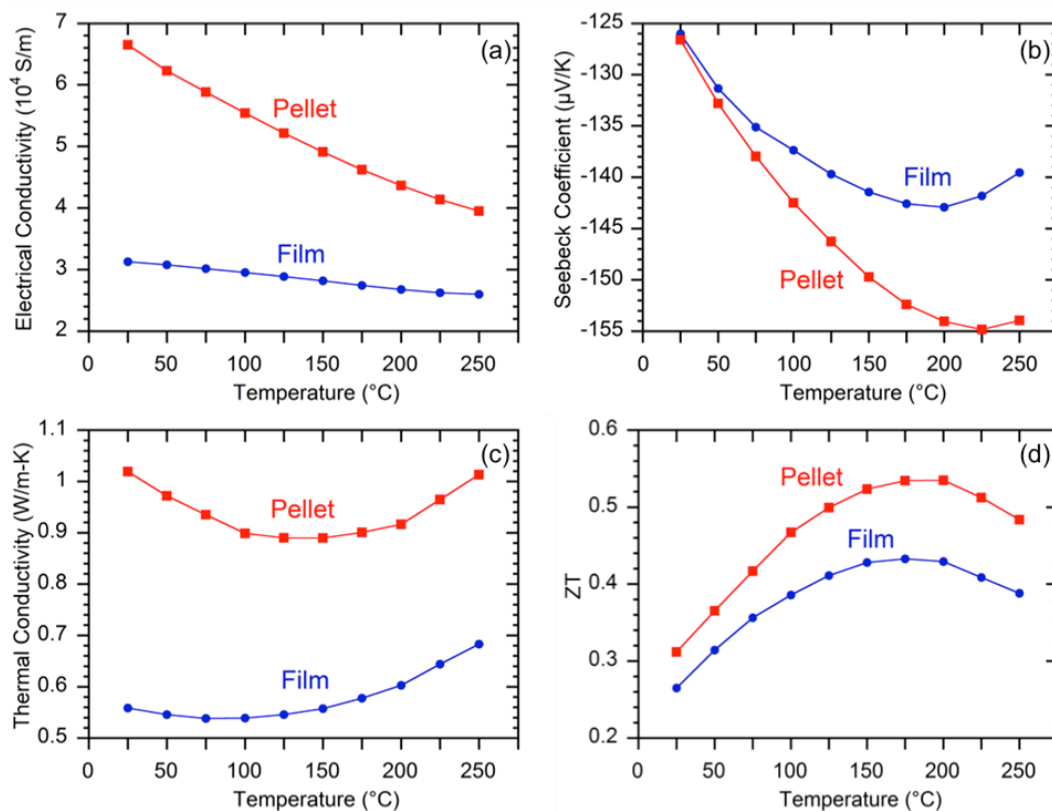


**Figure 51: Temperature-dependent (a) Electrical conductivity (b) Seebeck coefficient (c) Thermal conductivity and (d) ZT of a control pellet and flexible film**

Table 3 compares the peak ZT of several n-type thermoelectric materials. If the peak ZT is not available, the room temperature ZT is shown. As can be seen, all previously reported bismuth telluride based materials, which use a printing fabrication method, are much lower. In addition to exhibiting such a high ZT,  $\text{Bi}_2\text{Te}_{2.8}\text{Se}_{0.2}$  thick films are stable in air and exhibit the same thermoelectric properties regardless of thicknesses ranging from tens to hundreds of micrometers.

**Table 3: Thermoelectric performance literature comparison**

Materials details	Power factor (mW/mK <sup>2</sup> )	Peak/room T* ZT	Ref.	Fabrication methods
Bi <sub>2</sub> Te <sub>2.8</sub> Se <sub>0.2</sub>	0.56	0.43	(Ours)	Screen printing
Bi <sub>2</sub> Te <sub>3</sub>	1.33	0.35*	[16]	Screen printing
Bi <sub>2</sub> Te <sub>3</sub> +Epoxy	0.28	0.31*	[15]	Dispenser printing
CNT	0.15	N.A.	[23]	Drop casting
WS <sub>2</sub>	0.007	N.A.	[24]	Vacuum filtration
TiS <sub>2</sub> -Polymer	0.45	0.28	[25]	Electrochemical intercalation
CNT-PEDOT-TDAE	1.05	~0.5*	[26]	Spraying and spin coating

## CHAPTER 4: CONCLUSIONS AND FUTURE WORK

### 4.1 Conclusions

#### 4.1.1 Thermal Conductivity Measurement

Success was achieved in measuring the thermal conductivity of 700  $\mu\text{m}$  thick  $\text{Bi}_2\text{Te}_{2.8}\text{Se}_{0.8}$  films by using the parallel thermal conductance method. In order to use this method, samples needed a thickness greater than several tens of micrometers. Flexible thick film samples closer to 10-20  $\mu\text{m}$  were unable to be accurately measured due to the low sensitivity of the existing measurement set-up. Using 0.003" diameter thermocouples provided adequate sensitivity for temperature measurements of paste pellets while also neglecting the amount of heat conduction losses through the thermocouples and four heater wires. However, when measuring flexible thick film samples, the heat conduction losses through all metal wires and thermocouples could not be neglected.

The parallel thermal conductance method was an ideal starting point for measuring the thermal conductivity of various thermoelectric samples due to its ease of use. Unlike the  $3\omega$  method, photolithography or other clean-room processing procedures were unnecessary to carry out this measurement. In addition, the thermocouples, strain gage heater, silver paint thermal contacts, kapton support structure, and sample were the only variables that could alter the experimental results. Therefore, it was possible to analyze one variable at a time and determine how to improve the measurement

sensitivity. Ultimately, it was determined that the diameter of the thermocouples affected the parallel thermal conductance measurement the most.

#### 4.1.2 Seebeck Coefficient and Electrical Conductivity Measurements

##### 4.1.2.1 Spin Coated Thin Films

Initially, the electrical and thermal contacts between the LSR thermocouples and sample surface needed to be improved. Various experiments were performed in order to improve this contact using graphite foil and liquid graphite spray.

Most of the focus throughout this study was on the thermoelectric properties of  $\text{Cu}_2\text{Se}$ . Although  $\text{Bi}_2\text{Te}_3$  and  $\text{Cu}_2\text{S}$  samples were also measured, it was found that the most promising results for a publication were exhibited in  $\text{Cu}_2\text{Se}$ . Overall, as the annealing temperature increased, the Seebeck coefficient would also increase while the electrical conductivity would decrease. This decrease in the electrical conductivity could be attributed to a decrease in the charge carrier mobility. Multiple temperature profile tests had to be performed since test 1 was always different from test 2 and 3. It is hypothesized that  $\text{Cu}_2\text{Se}$  is a material that initially exhibits unstable thermoelectric properties when exposed to an electrical field and elevated temperature. It was determined that  $\text{Cu}_2\text{Se}$  annealed at  $430^\circ\text{C}$  had the highest power factor of  $0.62 \text{ mW/mK}^2$  at a temperature of  $411^\circ\text{C}$ . Determination of the actual peak power factor was not found due to the need to measure the sample at a temperature higher than the annealing temperature. This would result in additional sintering of the sample, thus changing the thermoelectric properties.

#### 4.1.2.2 Screen Printed Thick Films

The first step in optimizing the thermoelectric properties of  $\text{Bi}_2\text{Te}_{2.8}\text{Se}_{0.2}$  thick films was to determine the ideal annealing temperature. A temperature range between  $420^\circ\text{C}$  and  $450^\circ\text{C}$  was chosen based on the melting temperature of the polyimide substrate. Comparison of samples annealed at  $420^\circ\text{C}$ ,  $430^\circ\text{C}$ ,  $440^\circ\text{C}$ , and  $450^\circ\text{C}$  for 15 minutes resulted in the highest power factor of  $0.49 \text{ mW/mK}^2$  at  $186^\circ\text{C}$  for samples annealed at  $430^\circ\text{C}$ . An annealing temperature of  $430^\circ\text{C}$  allowed the  $\text{Bi}_2\text{Te}_{2.8}\text{Se}_{0.2}$  nanoplates to sinter and improve connections between the nanoplates without evaporating enough tellurium to decrease the carrier concentration.

From there, samples were annealed at  $430^\circ\text{C}$  for time durations of 15, 30, 45, 60, and 90 minutes. The Seebeck coefficient and electrical conductivity of these samples were initially measured using a custom-built testing system. Therefore, only the most promising samples were measured using the LSR. Samples annealed for 45 minutes exhibited a peak power factor of  $0.56 \text{ mW/mK}^2$  at  $186^\circ\text{C}$ .

### **4.2 Future Work**

#### 4.2.1 Thermal Conductivity Measurement

Thermal conductivity measurements are the most difficult thermoelectric property to accurately measure for thick and thin films. Various heat conduction losses affect the sensitivity of the measurement and can be difficult to avoid depending on what type of measurement method is selected.

When using a thermocouple based steady-state method, the amount of heat conduction losses are intrinsically higher than the alternative optical method. Therefore, selecting a hot side thermocouple diameter smaller than  $0.003''$  may help to further

minimize heat conduction losses. Other heat conduction losses may be due to the four lead wires that attach to the strain gage heater. Selecting a material with a lower thermal conductivity and comparable electrical conductivity may further reduce heat conduction losses. Decreasing the lead wire diameter may not be possible since wires with a diameter less than 0.003” are fragile, making it extremely difficult to mount a sample without damaging the rest of the set-up. Since the parallel thermal conductance method requires two measurements, the set-up should be disturbed as little as possible. Thus, broken lead wires in between measurement set-ups are not ideal and may alter the final measurement.

In order to successfully measure a thick flexible thermoelectric film, the film thickness may also need to be increased. Although the thinnest available polyimide substrate is 25  $\mu\text{m}$  with a thermal conductivity of 0.12 W/mK, the screen printed  $\text{Bi}_2\text{Te}_{2.8}\text{Se}_{0.2}$  films are closer to 10 or 20  $\mu\text{m}$ . As a result, the  $\text{Bi}_2\text{Te}_{2.8}\text{Se}_{0.2}$  films are not thick enough to produce an accurate thermal conductance reading. As seen with the previously reported results for a  $\text{Bi}_2\text{Te}_{2.8}\text{Se}_{0.2}$  paste pellet, a thickness of 700  $\mu\text{m}$  can successfully be measured. In addition, it may be worthwhile to perform a study on how thermocouple contact can influence the thermal conductivity results for various sample lengths.

If a thermocouple based thermal conductivity measurement method is not able to obtain accurate in-plane results for thick or thin films, it is suggested to explore alternative measurement methods. Using a variable linewidth  $3\omega$  method with a wide and narrow heating strip can be used to measure both the cross-plane and in-plane thermal conductivity [48]. This method does, however, require more intensive sample preparation since the heating strips are typically deposited onto the sample surface using

photolithography in order to achieve a sufficiently narrow heater. The wide heater is used to determine the cross-plane thermal conductivity while the narrow heater determines the in-plane thermal conductivity. It is also important to keep in mind that measuring the thermal conductivity of supported films tend to result in less sensitive measurements compared to suspended film measurement methods.

#### 4.2.2 Design of Thermoelectric Device

This study has proven that the LSR is capable of measuring films as thin as 60 nm. Once the thermal conductivity of thick screen printed films can be successfully measured, the next step is to design a thermoelectric device. In order to make a wearable device that can be used for biomedical applications, heat transfer must be improved between the thermoelectric device and skin. In addition, the power density of the device must also be optimized.

The initial stage of this phase is to develop device designs and run simulations using ANSYS. ANSYS is a finite element and thermal analysis software. Using ANSYS during the modeling stage will allow for better understanding of how to maximize the cold side temperature, study the heat transfer between the device and skin, and optimize the device power density.

Once the modeling phase is complete, a flexible device can be fabricated. The device will then be tested on its bending properties and power performance. Creation of a stretchable, wearable device is a relatively new field, which could significantly contribute to the world of medical devices.

## REFERENCES

1. Bahk, J.H., et al., *Flexible thermoelectric materials and device optimization for wearable energy harvesting*. Journal of Materials Chemistry C, 2015. **3**(40): p. 10362-10374.
2. Haahr, R.G., et al. *A wearable "electronic patch" for wireless continuous monitoring of chronically diseased patients*. IEEE.
3. Son, D., et al., *Multifunctional wearable devices for diagnosis and therapy of movement disorders*. Nature Nanotechnology, 2014. **9**(5): p. 397-404.
4. Sun, M.G., et al., *A Wearable Electronic System for Objective Dietary Assessment*. Journal of the American Dietetic Association, 2010. **110**(1): p. 45-47.
5. Bin-Mahfoodh, M., et al., *Longevity of batteries in internal pulse generators used for deep brain stimulation*. Stereotactic and Functional Neurosurgery, 2003. **80**(1-4): p. 56-60.
6. Rasouli, M. and L.S.J. Phee, *Energy sources and their development for application in medical devices*. Expert Review of Medical Devices, 2010. **7**(5): p. 693-709.
7. Schwalb, J.M. and C. Hamani, *The history and future of deep brain stimulation*. Neurotherapeutics, 2008. **5**(1): p. 3-13.
8. Karami, M.A. and D.J. Inman, *Powering pacemakers from heartbeat vibrations using linear and nonlinear energy harvesters*. Applied Physics Letters, 2012. **100**(4).
9. Wong, L.S.Y., et al., *A very low-power CMOS mixed-signal IC for implantable pacemaker applications*. Ieee Journal of Solid-State Circuits, 2004. **39**(12): p. 2446-2456.
10. Ohm, O.J. and D. Danilovic, *Improvements in pacemaker energy consumption and functional capability: four decades of progress*. Pacing and clinical electrophysiology, 1997. **20**(1): p. 2-9.
11. Mitcheson, P.D., et al., *Energy harvesting from human and machine motion for wireless electronic devices*. Proceedings of the Ieee, 2008. **96**(9): p. 1457-1486.
12. Mond, H.G. and A. Proclemer, *The 11th World Survey of Cardiac Pacing and Implantable Cardioverter-Defibrillators: Calendar Year 2009-A World Society of Arrhythmia's Project*. Pace-Pacing and Clinical Electrophysiology, 2011. **34**(8): p. 1013-1027.
13. Tashiro, R., et al., *Development of an electrostatic generator for a cardiac pacemaker that harnesses the ventricular wall motion*. Journal of Artificial Organs, 2002. **5**(4): p. 0239-0245.
14. Sarpeshkar, R., *Ultra-Low Power Bioelectronics. 1*. 2010, Cambridge University Press.

15. Yang, Y., X.-J. Wei, and J. Liu, *Suitability of a thermoelectric power generator for implantable medical electronic devices*. Journal of Physics D: Applied Physics, 2007. **40**(18): p. 5790.
16. Wei, X. and J. Liu, *Power sources and electrical recharging strategies for implantable medical devices*. Frontiers of Energy and Power Engineering in China, 2008. **2**(1): p. 1-13.
17. Roundy, S., et al. *Power sources for wireless sensor networks*. Springer.
18. Cadei, A., et al., *Kinetic and thermal energy harvesters for implantable medical devices and biomedical autonomous sensors*. Measurement Science and Technology, 2014. **25**(1): p. 14.
19. Romero, E., R.O. Warrington, and M.R. Neuman, *Energy scavenging sources for biomedical sensors*. Physiological Measurement, 2009. **30**(9): p. R35-R62.
20. Roundy, S. and P.K. Wright, *A piezoelectric vibration based generator for wireless electronics*. Smart Materials and structures, 2004. **13**(5): p. 1131.
21. Williams, C.B., et al., *Development of an electromagnetic micro-generator*. Iee Proceedings-Circuits Devices and Systems, 2001. **148**(6): p. 337-342.
22. Beeby, S.P., et al., *A micro electromagnetic generator for vibration energy harvesting*. Journal of Micromechanics and microengineering, 2007. **17**(7): p. 1257.
23. Sari, I., T. Balkan, and H. Kulah, *An electromagnetic micro power generator for wideband environmental vibrations*. Sensors and Actuators A: Physical, 2008. **145**: p. 405-413.
24. Paracha, A.M., et al., *A high power density electrostatic vibration-to-electric energy converter based on an in-plane overlap plate (IPOP) mechanism*. arXiv preprint arXiv:0802.3063, 2008.
25. Menger, S., et al., *Vibration-to-electric energy conversion*. Ieee Transactions on Very Large Scale Integration (Vlsi) Systems, 2001. **9**(1): p. 64-76.
26. Tashiro, R., et al., *Development of an electrostatic generator that harnesses the motion of a living body (use of a resonant phenomenon)*. Jsme International Journal Series C-Mechanical Systems Machine Elements and Manufacturing, 2000. **43**(4): p. 916-922.
27. Leonov, V., *Energy harvesting for self-powered wearable devices*, in *Wearable Monitoring Systems*. 2011, Springer. p. 27-49.
28. Kim, S.J., J.H. We, and B.J. Cho, *A wearable thermoelectric generator fabricated on a glass fabric*. Energy & Environmental Science, 2014. **7**(6): p. 1959-1965.
29. Tian, Z., S. Lee, and G. Chen, *A comprehensive review of heat transfer in thermoelectric materials and devices*. Ann. Rev. Heat Transfer, 2014. **17**: p. 425-483.
30. Rowe, D.M., *Thermoelectrics handbook: macro to nano*. 2005: CRC press.
31. Riffat, S.B. and X.L. Ma, *Thermoelectrics: a review of present and potential applications*. Applied Thermal Engineering, 2003. **23**(8): p. 913-935.
32. Po, J.M., et al., *Measurement of the dopant concentration in a semiconductor using the Seebeck effect*. Measurement Science and Technology, 2013. **24**(5).
33. Zhang, Y., *Thermal and thermoelectric transport in nanostructured materials from pnictogen chalcogenide nanoplate crystals*. 2011.

34. Gao, X., et al., *Rational design of high-efficiency thermoelectric materials with low band gap conductive polymers*. Computational Materials Science, 2006. **36**(1-2): p. 49-53.
35. Glosch, H., et al., *A thermoelectric converter for energy supply*. Sensors and Actuators a-Physical, 1999. **74**(1-3): p. 246-250.
36. Nolas, G.S., J. Sharp, and J. Goldsmid, *Thermoelectrics: basic principles and new materials developments*. 2013: Springer Science & Business Media.
37. Sootsman, J.R., D.Y. Chung, and M.G. Kanatzidis, *New and Old Concepts in Thermoelectric Materials*. Angewandte Chemie International Edition, 2009. **48**(46): p. 8616-8639.
38. Boffoué, O., et al., *Experimental setup for the measurement of the electrical resistivity and thermopower of thin films and bulk materials*. Review of Scientific Instruments, 2005. **76**(5): p. 053907.
39. Bahk, J.-H., T. Favalaro, and A. Shakouri, *Thin film thermoelectric characterization techniques*. Annual Review of Heat Transfer, 2013. **16**(1).
40. Schroder, D.K., *Semiconductor material and device characterization*. 2006: John Wiley & Sons.
41. Nalwa, H.S., *Handbook of Thin Films, Five-Volume Set*. 2001: Academic Press.
42. Wieder, H.H., *Laboratory notes on electrical and galvanomagnetic measurements*. Materials science monographs. 1979, Amsterdam, New York: Elsevier Scientific Pub. Co., distributors for the U.S. and Canada, Elsevier/North-Holland.
43. Valdes, L.B., *RESISTIVITY MEASUREMENTS ON GERMANIUM FOR TRANSISTORS*. Proceedings of the Institute of Radio Engineers, 1954. **42**(2): p. 420-427.
44. Matsumura, T. and Y. Sato, *A theoretical study on Van der Pauw measurement values of inhomogeneous compound semiconductor thin films*. Journal of Modern Physics, 2010. **1**(05): p. 340.
45. Pm, N.O., *A method of measuring the resistivity and Hall coefficient on lamellae of arbitrary shape*. 1958.
46. Zawilski, B.M., R.T. Littleton, and T.M. Tritt, *Description of the parallel thermal conductance technique for the measurement of the thermal conductivity of small diameter samples*. Review of Scientific Instruments, 2001. **72**(3): p. 1770-1774.
47. Wan, C.L., et al., *Flexible n-type thermoelectric materials by organic intercalation of layered transition metal dichalcogenide  $TiS_2$* . Nature Materials, 2015. **14**(6): p. 622-627.
48. Dames, C., *Measuring the thermal conductivity of thin films: 3 omega and related electrothermal methods*. Annual Review of Heat Transfer, 2013. **16**(16).
49. Liu, W.L., et al., *Anisotropic thermal conductivity of Ge quantum-dot and symmetrically strained Si/Ge superlattices*. Journal of Nanoscience and Nanotechnology, 2001. **1**(1): p. 39-42.
50. Ju, Y.S., K. Kurabayashi, and K.E. Goodson, *Thermal characterization of anisotropic thin dielectric films using harmonic Joule heating*. Thin Solid Films, 1999. **339**(1-2): p. 160-164.

51. Cahill, D.G., et al., *THERMAL-CONDUCTIVITY OF THIN-FILMS - MEASUREMENTS AND UNDERSTANDING*. Journal of Vacuum Science & Technology a-Vacuum Surfaces and Films, 1989. **7**(3): p. 1259-1266.
52. Paddock, C.A. and G.L. Eesley, *TRANSIENT THERMOREFLECTANCE FROM THIN METAL-FILMS*. Journal of Applied Physics, 1986. **60**(1): p. 285-290.
53. Garrelts, R., A. Marconnet, and X.F. Xu, *ASSESSMENT OF THERMAL PROPERTIES VIA NANOSECOND THERMOREFLECTANCE METHOD*. Nanoscale and Microscale Thermophysical Engineering, 2015. **19**(4): p. 245-257.
54. Lin, Z.Y., et al., *Solution Processable Colloidal Nanoplates as Building Blocks for High-Performance Electronic Thin Films on Flexible Substrates*. Nano Letters, 2014. **14**(11): p. 6547-6553.
55. Liu, H.L., et al., *Copper ion liquid-like thermoelectrics*. Nature Materials, 2012. **11**(5): p. 422-425.
56. Mehta, R.J., et al., *A new class of doped nanobulk high-figure-of-merit thermoelectrics by scalable bottom-up assembly*. Nature Materials, 2012. **11**(3): p. 233-240.